

Distribution and Nature of Fault Architecture in a Layered Sandstone and Shale Sequence: An Example from the Moab Fault, Utah

N. C. Davatzes¹

Department of Geological and Environmental Science, Stanford University, Stanford, California, U.S.A.

A. Aydin

Department of Geological and Environmental Science, Stanford University, Stanford, California, U.S.A.

ABSTRACT

We examined the distribution of fault rock and damage zone structures in sandstone and shale along the Moab fault, a basin-scale normal fault with nearly 1 km (0.62 mi) of throw, in southeast Utah. We find that fault rock and damage zone structures vary along strike and dip. Variations are related to changes in fault geometry, faulted slip, lithology, and the mechanism of faulting. In sandstone, we differentiated two structural assemblages: (1) deformation bands, zones of deformation bands, and polished slip surfaces and (2) joints, sheared joints, and breccia. These structural assemblages result from the deformation band-based mechanism and the joint-based mechanism, respectively. Along the Moab fault, where both types of structures are present, joint-based deformation is always younger. Where shale is juxtaposed against the fault, a third faulting mechanism, smearing of shale by ductile deformation and associated shale fault rocks, occurs. Based on the knowledge of these three mechanisms, we projected the distribution of their structural products in three dimensions along idealized fault surfaces and evaluated the potential effect on fluid and hydrocarbon flow. We contend that these mechanisms could be used to facilitate predictions of fault and damage zone structures and their permeability from limited data sets.

¹*Present address:* Earthquake Hazards Team, U.S. Geological Survey, Menlo Park, California, U.S.A.

INTRODUCTION

Faults can act as highly permeable pathways that enhance fluid flow parallel to faults, low-permeability zones that inhibit fluid flow across faults, or complex conduit-barrier systems (Bredehoeft et al., 1982) that evolve temporally (Sibson, 1990; Caine et al., 1996) and spatially (Caine and Forster, 1999; Davatzes, 2003). This behavior is evident from field observations of localized diagenesis that indicates focused fluid flow along faults (Dholakia et al., 1998; Nelson et al., 1999; Sigda et al., 1999; Taylor et al., 1999; Eichhubl and Boles, 2000) or barrier behavior that inhibited cross-fault flow (Antonellini and Aydin, 1994, 1995; Antonellini et al., 1999; Aydin, 2000). The permeability of a fault is related to its architecture, i.e., the type, geometry, distribution, and density of structures composing a fault zone (Knipe, 1993; Caine et al., 1996; Heynekamp et al., 1999). Many authors (Matthai et al., 1998; Caine and Forster, 1999; Flodin et al., 2001; Jourde et al., 2002) have used the geometry and connectivity of fault zone structures with distinct hydrologic properties to determine the equivalent bulk (upscaled) permeability of a fault zone. Thus, predicting the distribution of different structures along a fault zone is a key step in predicting the overall permeability structure of a fault.

Along the Moab fault system, southeast Utah, we recognized three distinct sets of structures that might impact the function of the fault in fluid flow. Joints, networks of joints, and breccia may enhance permeability by introducing zones of increased secondary porosity that are well connected (Dholakia et al., 1998; Caine and Forster, 1999; Taylor et al., 1999; Flodin et al., 2001; Davatzes and Aydin, 2003). Conversely, in sandstone adjacent to the fault, cataclastic deformation bands are zones of well-connected porosity reduction that could reduce permeability (Foxford et al., 1998; Davatzes and Aydin, 2003). In general, joints always overprint deformation bands along the Moab fault system. The overprinting indicates a temporal change in the faulting mechanisms and resulting structures that comprise the fault and, consequently, a corresponding change in the fault zone permeability. Finally, clay or shale generally has low permeability (Skerlec, 1999) and is abundant along the Moab fault. Thus, incorporating these materials into or adjacent to a fault zone impacts the fault-parallel and fault-normal permeability (Weber et al., 1978; Lehner and Pilaar, 1991, 1997; Lindsay et al., 1993; Knipe, 1997; Caine and Forster, 1999; Sigda et al., 1999). This effect may be enhanced by foliation and gouge formation from shale-rich rocks and shale smear along the fault zone (Knipe 1993, 1997; Gibson, 1994; Faulkner and Rutter, 1998).

Traditional approaches to characterizing the cross-fault sealing potential of a fault zone have primarily focused on the function of low-permeability rocks jux-

taped against high-permeability rocks across a fault (Allan, 1989; Knipe, 1997) and the potential for shale-rich fault rocks to occur in the fault zone (Yielding et al., 1997). These methods include the following:

- 1) Juxtaposition analysis: This method assumes that the fault has no hydraulic properties, but sealing may result from the juxtaposition of low-permeability rocks (e.g., shale) against high-permeability rocks (Allan, 1989; Knipe, 1997).
- 2) Shale smear factor: This method compares the thickness of shale units in a faulted interval to the critical throw at which shale is no longer present in the fault zone (Lindsay et al., 1993; Gibson, 1994; Aydin and Eyal, 2002).
- 3) Shale gouge ratio: This ratio is calculated as the cumulative thickness of shale units in the faulted interval divided by the throw (Fristad et al., 1997; Yielding et al., 1997). Sealing is determined by calibrating this number to subsurface data on pore pressure differences across faults in the subsurface. Sealing is typically considered when the cumulative thickness of shale units in the faulted interval is about 18–20% of the throw.
- 4) Smear gouge ratio: This is the ratio between sand and shale in the faulted interval and is similar to the shale gouge ratio (Skerlec, 1999).
- 5) Statistical data sets based on subsurface estimates or outcrop analogs (e.g., Foxford et al., 1998).

However, none of these methods adequately consider and justify the physical processes responsible for fault development or consider the possibility of enhanced flow in the fault zone. In this contribution, we explore the benefits of using faulting processes to analyze, extrapolate, or predict fault characteristics in combination with other commonly cited geometric parameters.

We propose that three factors control the development of fault architecture along a fault in a layered sandstone and shale sequence: (1) the relative contributions of different faulting mechanisms to fault growth and slip; (2) the geometry of the fault; (3) the distribution of rock types. We quantified the relationships between these three factors along the Moab normal fault system. The architecture of this fault system in Jurassic sandstone units has been extensively characterized in previous work (Foxford et al., 1996, 1998; Davatzes, 2003; Davatzes and Aydin, 2003). However, the effect of shale on the architecture of the Moab fault has not been adequately investigated. In this study, we quantify the behavior of shale in the Moab fault zone and integrate these results with the previous results in sandstone to determine the three-dimensional architecture of the Moab fault. Our results demonstrate that despite the complexity of the Moab fault, fault zone structures are distributed in a consistent pattern determined by the

FIGURE 1. Tectonic map of part of the northeast Paradox basin in eastern Utah (modified from Doelling, 1988).

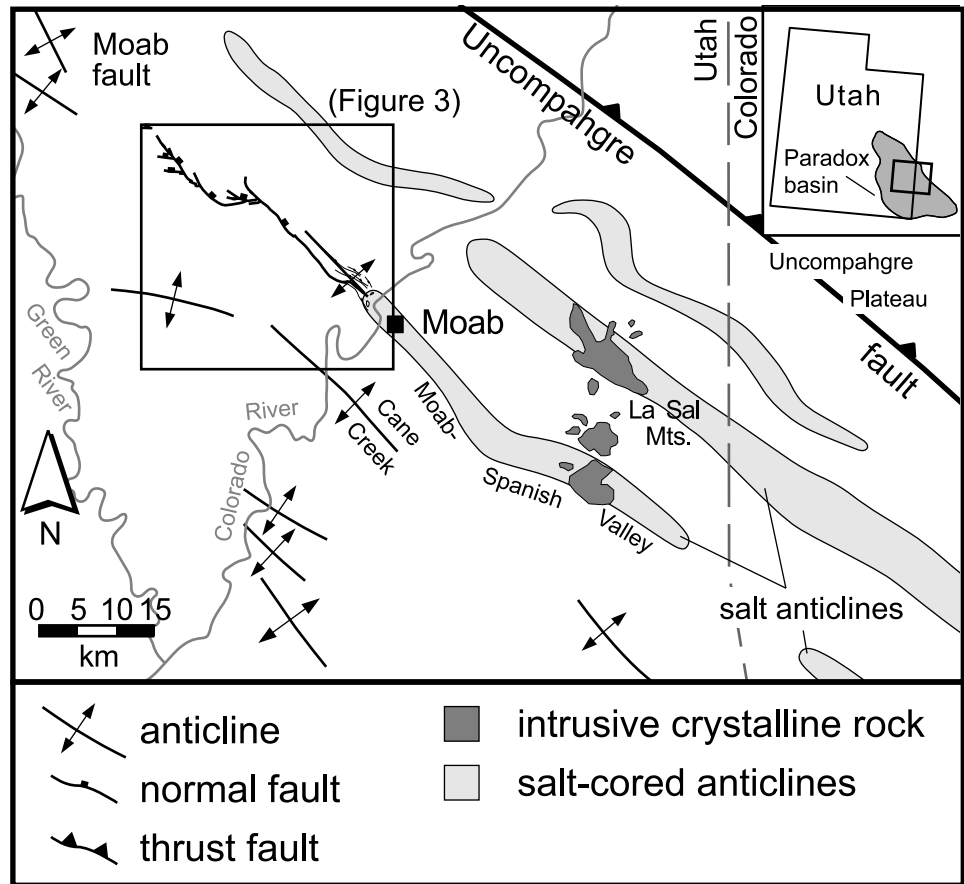
influence of the faulted stratigraphy, slip distribution, and fault geometry on the mechanisms of faulting.

GEOLOGIC SETTING

The Moab fault system is a basin-scale normal fault, approximately 45 km (28 mi) long, with nearly 1 km (0.62 mi) of throw located in the northeastern part of the Paradox basin in southeast Utah (Figure 1). The fault crops out in Pennsylvanian to Cretaceous stratigraphy overlying the Paradox Salt Formation (Figure 2). The southeastern part of the Moab fault (Figure 3) exposes stratigraphic units dominantly composed of interbedded sandstone and shale in varying ratios. These units include the Honaker Trail, Cutler, Moenkopi, and Chinle formations in the footwall and the Salt Wash Member of the Morrison Formation in the hanging wall (Figure 2).

Exposures along the northwestern extent of the Moab fault system are limited to Jurassic and younger units (Figure 3). The stratigraphy in this region is dominated by an abrupt change from a thick package of eolian sandstone units, including the Wingate, Kayenta, Navajo, and Entrada formations (Figure 2), to a shale-dominated sequence that includes the Late Jurassic Morrison Formation and the Cretaceous Cedar Mountain, Dakota Formation, and Mancos Shale. The sandstone units typically have high porosities from 15 to 25% (Dyer, 1983; Antonellini and Aydin, 1994; Foxford et al., 1996) and are exposed in the footwall, whereas the shale units are exposed primarily in the hanging wall, although the Tidwell and Salt Wash Members of the Morrison Formation intermittently crop out in the footwall along the fault as well. In these shale-dominated units, stratigraphic boundaries are demarcated by prominent, but relatively thin, sandstone layers.

Most of the data on the shale in the fault zone that are presented in this study are derived from observations



in the Morrison Formation (Doelling, 1982, 1988), which is divided into three members. The Tidwell Member was deposited in quiet, shallow water on the margin of a flood plain and is composed of shale with some siltstone, limestone, and chert-bearing layers. The Salt Wash Member is a fluvial deposit dominated by overbank mud with channel sand deposits, forming sandstone sheets of highly variable thickness. Three to five sandstone layers occur in the shale and may range in thickness from 1 to 20 m (3 to 66 ft) but are typically 3–5 m (10–16 ft) thick. Finally, in the study area, the Brushy Basin Member is a distal flood-plain, shale-dominated deposit with isolated, coarse, and incised-channel sandstones. Ash layers make this unit rich in swelling clays such as smectite.

Faulting in the study area probably occurred between 60 and 43 Ma based on K-Ar dating of shale gouge in the Morrison Formation (Pevear et al., 1997; and other arguments summarized in Davatzes and Aydin, 2003). The faulting was associated with a period of salt movement (Doelling, 1988) during the Laramide orogeny and either occurred during maximum burial of the Entrada formation to a depth between 2000 and 2500 m (6600 and 8200 ft) (Pevear et al., 1997; Garden et al., 2001) or during a phase of subsidence immediately preceding maximum burial (Nuccio and Condon, 1996). Faulting possibly extended into the period of rapid uplift and exhumation following maximum burial.

FAULTING MECHANISMS, TERMINOLOGY, AND FIELD METHODS

Following previous workers, we divide the fault zone into a central core that accommodates the majority of offset and is bounded on either side by damage zones (Sibson, 1977; Chester and Logan, 1986; Caine et al., 1996). In this chapter, we use the term “fault rock” as a general term for all highly deformed rocks that comprise the fault core. Structures in the fault core and damage zone are associated with three distinct faulting mechanisms that evolve with increasing offset (Figure 4).

Faults that cut sandstone units along the Moab fault are comprised of two distinct sets of structures that result from different faulting mechanisms (see Davatzes and Aydin, 2003, for a detailed discussion). Cataclastic deformation bands, zones of deformation bands, and slip surfaces are products of the deformation band-based faulting mechanism (Figure 4a) (Aydin and Johnson, 1978; Antonellini and Aydin, 1994). This mechanism involves grain crushing and pore collapse in tabular zones a few millimeters thick, single deformation bands that each accommodate 1–10 mm (0.04–0.4 in.) of shear displacement.

In contrast, joints, sheared joints, splay fractures, zones of fragmented rock, and breccia are products of the joint-based mechanism (Figure 4b) (Myers, 1999; Flodin, 2003). This mechanism localizes shear across established discontinuities, such as joints, resulting in a stress perturbation at the tip of the sheared discontinuity (e.g., Anderson, 1995). Tensile quadrants of the stress perturbation promote the formation of new joints called splay fractures (e.g., Brace and Bombolakis, 1963). This mechanism proceeds by cyclic shearing of earlier joints and formation of new joints as splay fractures. Splay fractures are also known in the literature as secondary fractures, horsetail fractures, pinnate fractures, kink fractures, bridge fractures, and tail fractures (Segall and Pollard, 1980; Granier, 1985; Engelder, 1987; Martel, 1990; Cruikshank et al., 1991; Cruikshank and Aydin, 1994).

In layered sandstone and shale, a fault zone may be composed of smeared shale that remains continuous across the fault zone, sandwiched between brittle faults in surrounding sandstone units (Figure 4c) that form a relay. Smeared shale refers to the entire thickness of shale entrained in the fault core, including beds folded and attenuated parallel to fault slip surfaces as well as gouge (Weber et al., 1978; Lehner and Pilaar, 1997; Aydin and Eyal, 2002; Koledoye et al., 2003). Shale gouge refers to a fault rock consisting of the portion of entrained shale in which sedimentary layering is thoroughly disrupted and mixing may have occurred.

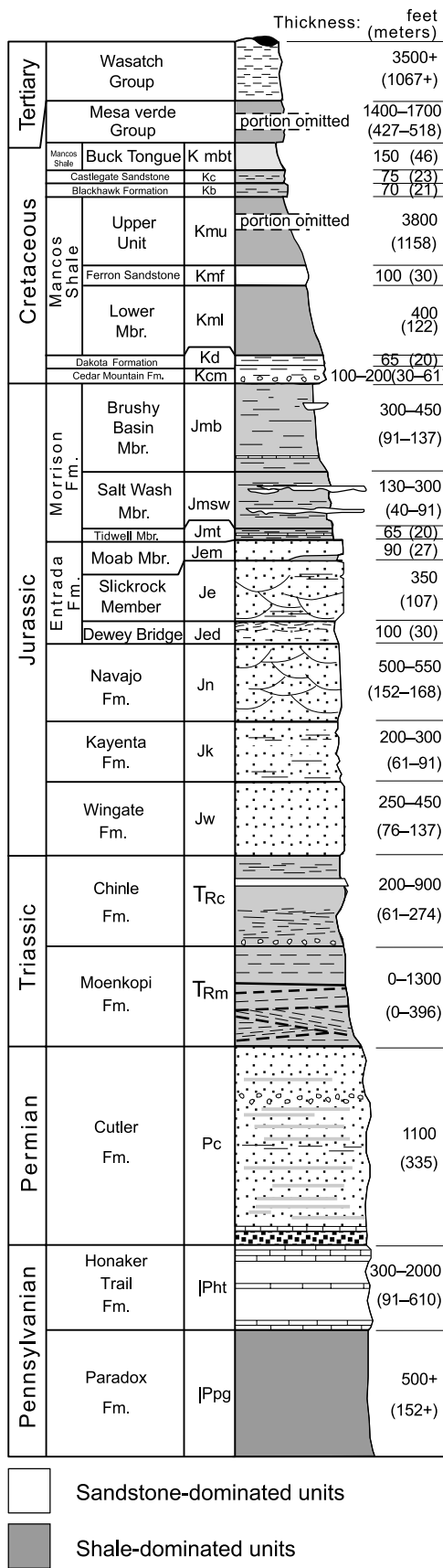


FIGURE 2. Stratigraphy of the study area (modified from Doelling, 1985).

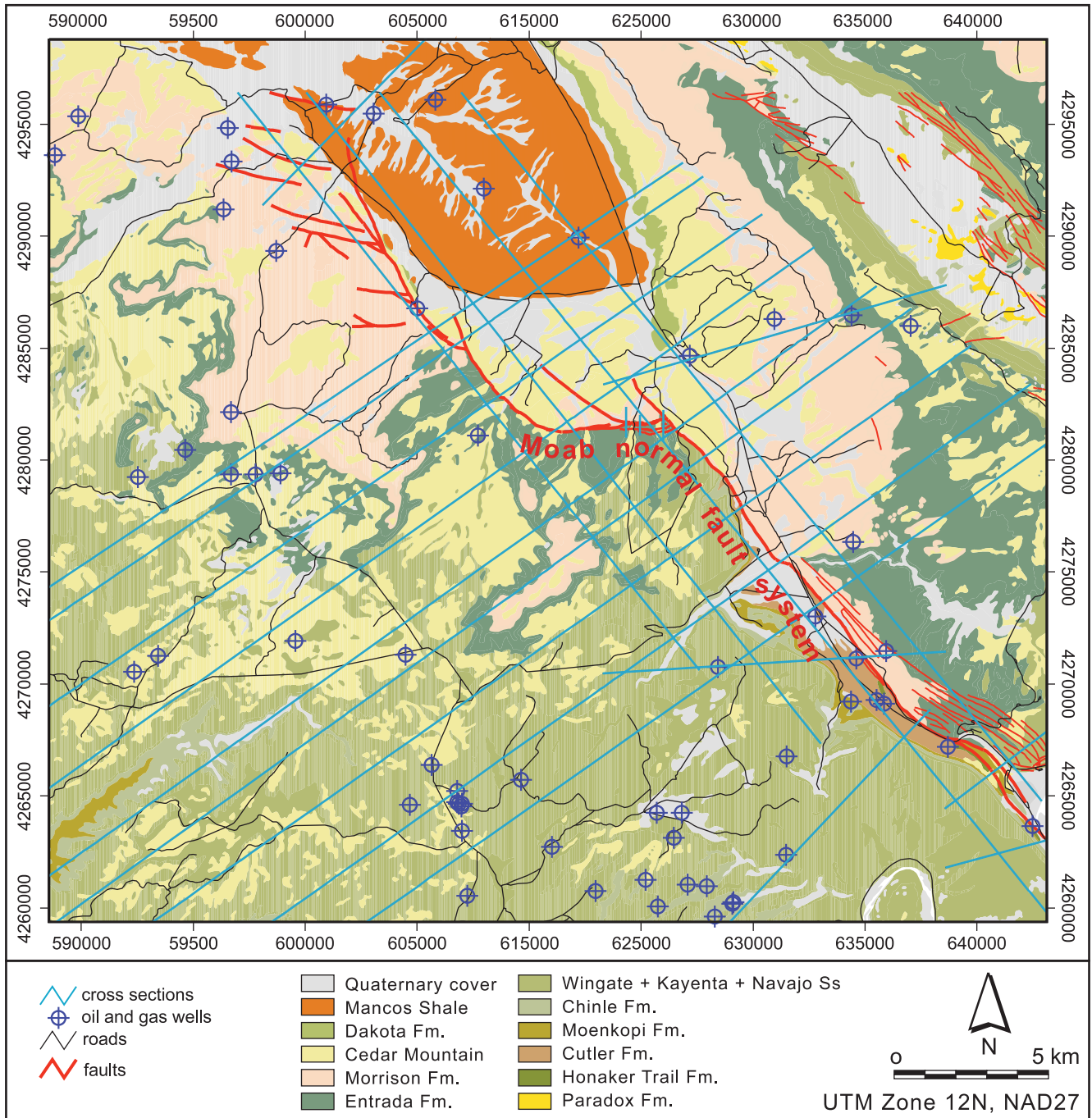


FIGURE 3. Geology of the Moab area including data sets used to constrain the three-dimensional fault geometry and stratigraphy. The basic geologic map was modified from Doelling (2002) by traditional mapping techniques and local GPS measurements. Map coordinates are Universal Transverse Mercator (UTM) zone 12, in the North American Datum established in 1927 (NAD27).

Data were collected in the field using several traditional methods. We conducted detailed outcrop mapping of fault zone structures, their distribution, relative geometry, and crosscutting relationship to infer the mechanisms of infaulting. Maps and cross sections were created using unrectified outcrop and rectified air photo base maps, global positioning surveying (GPS), and a

10-m (33-ft) resolution digital elevation model. We also quantified the thickness distribution of shale fault rocks in the fault zone using GPS data and a tape measure. We distinguished the source of shale fault rocks whenever possible. As a consequence of this analysis, we identified several parameters that appear to have controlled the distribution of fault zone structures.

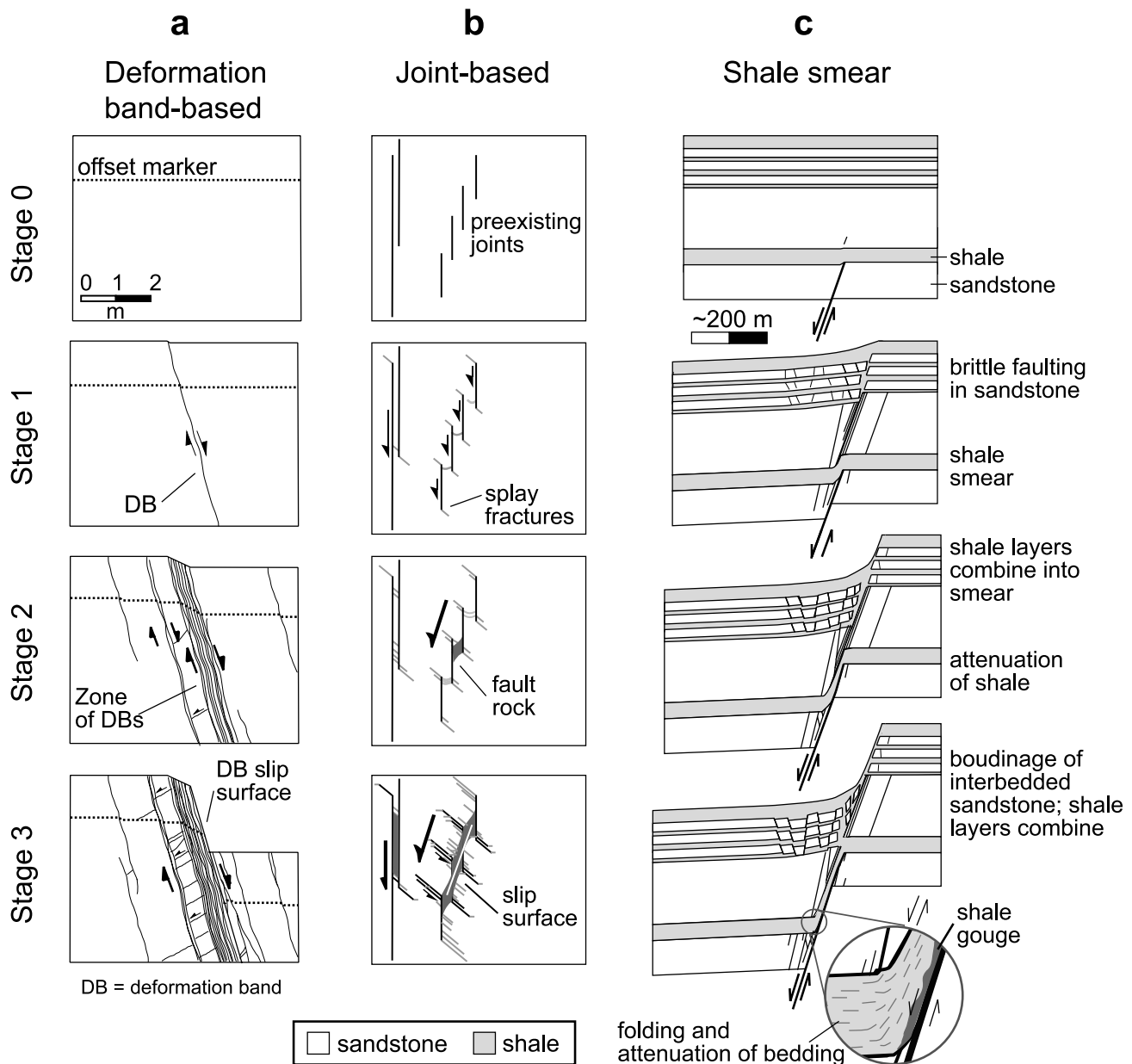


FIGURE 4. Evolution of fault architecture by brittle faulting mechanisms in sandstone including (a) deformation band-based (modified after Aydin and Johnson, 1978; Antonellini and Aydin, 1995) and (b) joint-based faulting (modified after Myers, 1999). (c) Evolution of fault architecture with shale smear includes ductile smearing of shale and brittle faulting in surrounding sandstone. The length scale in (b) is relative to the dimensions of the initial discontinuities. The length scale in (c) is relative to the shale bed thickness.

OBSERVATIONS AND RESULTS

Detailed Examples of Shale Deformation

Small faults in the Salt Wash Member demonstrate several key aspects of shale behavior in fault zones. First, despite brittle failure, indicated by deformation bands and some joints, in the surrounding sandstone layers (Figure 5), the shale units remain continuous from footwall to hanging wall, although they are drastically

thinned. As a result, the fault surface from the upper sandstone unit to the lower sandstone unit is discontinuous and forms a vertical relay. As the shale layer approaches the relay, its internal bedding rotates to be parallel with the fault surfaces in the relay. A thin sandstone bed in the shale layer is also rotated with the shale and accommodates extension and thinning by brittle faulting (hanging wall of fault in Figure 5). In this case, the sandstone bed provides a marker that indicates that shale has accommodated extension without brittle

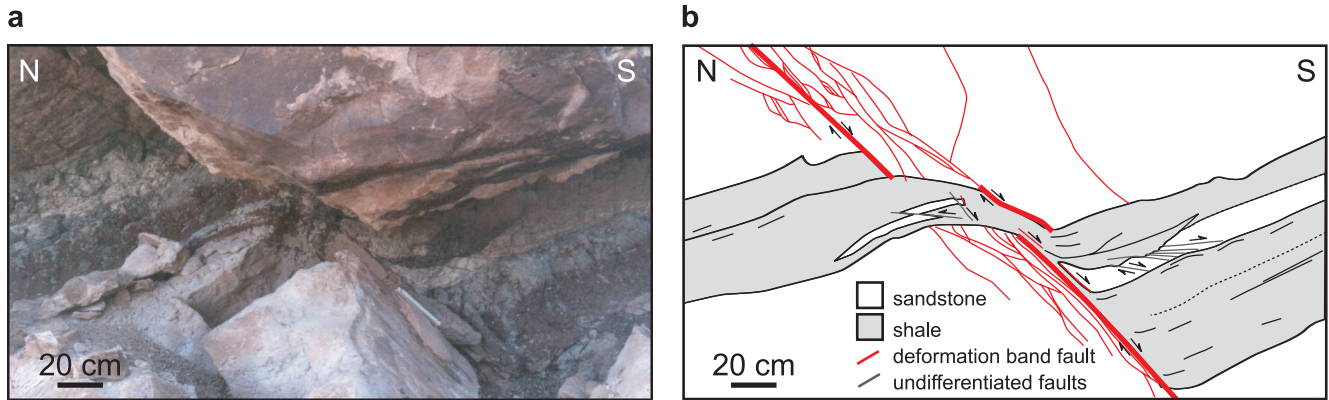


FIGURE 5. (a) Outcrop photo and (b) detailed cross section of small fault cutting coarse sandstone layers that sandwich a thinner shale layer, which is smeared through the relay in the Salt Wash Member. Outcrop located at $60^{\circ}96'84''\text{E}$, $42^{\circ}85'17.6''\text{N}$ (Zone 12N, NAD27).

faulting, and the relatively thin sandstone layer has been moved with the shale. The minimum thickness of shale in the fault zone inside the relay is 10 cm (4 in.) and is thickest near the source of shale. This geometry suggests that the accumulation of throw and the distance from the source of shale might have both affected the thickness of shale in the core of this fault.

Second, parts of the Moab fault with larger offset contain a thin seam of shale gouge in the fault core adjacent to the fault surface, where shale is juxtaposed against the fault (e.g., Figure 6a, b). Multiple shale beds merge with this gouge layer (Figure 6b) and thus appear to constitute sources of shale. In addition, sandstone beds sandwiched between these shale beds are faulted and extended. The interbedded shale layers remain continuous between the sandstone blocks but commonly appear thinned. As a result, many fault-bounded sandstone blocks form boudins surrounded by shale. Both sandstone boudins and shale beds are nearly parallel to the fault slip surface. This geometry suggests that the entire package of thinly interbedded sandstone and shale has been extended and potentially attenuated in the direction of slip as part of the fault core.

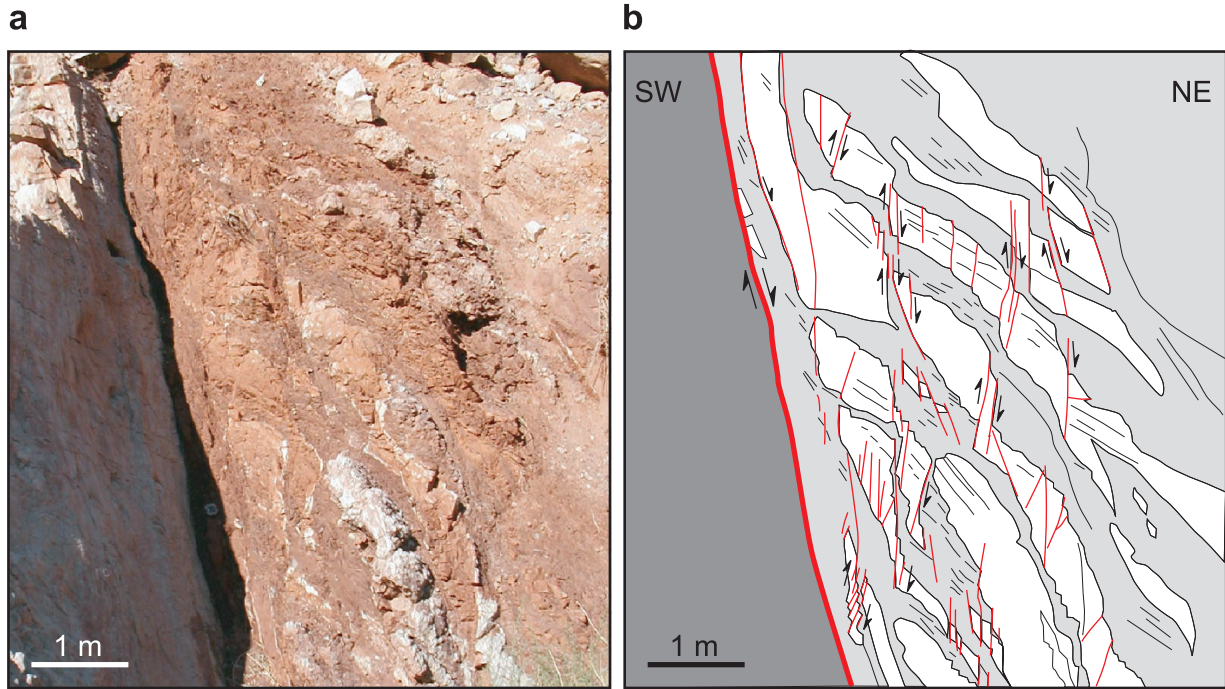
In Figure 6c and d, two distinct fault cores consist of smeared shale and breccia bounded by slip surfaces in sandstone layers that are thick relative to shale layers. The fault core in the upper center of Figure 6d is thickest where a shale layer enters the fault core near the top of the exposure. The increased thickness of the core in Figure 6d and the entrainment of multiple shale layers in Figure 6b are consistent with continual incorporation of additional shale layers into the fault core. Conversely, the shale in the fault core, in the center of Figure 6c and d, is thinnest at the lower corner of a thick, hanging-wall sandstone unit. This geometry appears to be related to resistance by the relatively thick sandstone layer to folding and boudinage (e.g., thin sandstone layers in Figure 6b). Such resistance might

limit rotation and cause the sandstone to impinge on the shale smear as the footwall and hanging wall slip past each other. Thus, the relative abundance and thickness of shale layers vs. sandstone layers might be a major factor in determining how shale is distributed in the fault core.

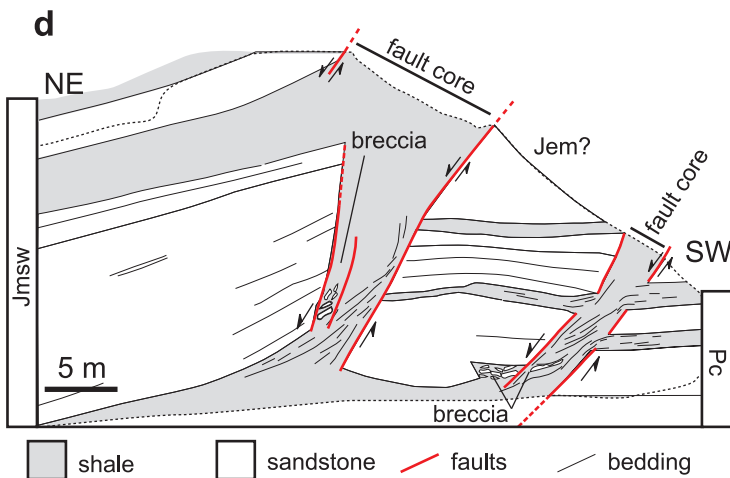
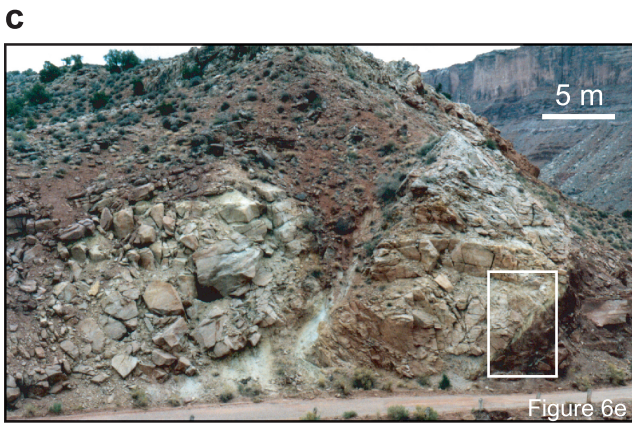
Geometry and Distribution of Shale in the Fault Zone

The northwestern part of the Moab fault system is characterized by folded shale units in the hanging wall juxtaposed against the thick sequence of Jurassic sandstone units in the footwall (Figure 7). Folds are asymmetric across the fault zone, with most of the change of bedding inclination in the hanging wall, whereas beds in the footwall exhibit the regional dip. In the hanging wall, the overall fold geometry is asymptotic; bed dip is greatest adjacent to the fault and approaches the regional dip over several hundred meters into the hanging wall (e.g., sections D, E, V, H, J3, L, and Q in Figure 7). This fold geometry broadens the area over which shale units in the hanging wall are juxtaposed against the fault core. In addition, sandstone marker beds in shale units converge as bed dip increases toward the fault over the length of these folds. This convergence indicates thinning of shale layers as they approach the fault core. Taken together, the rotation of bedding dip and thinning of shale into the fault core, which are absent in the footwall, might indicate that the shale in the fault core is preferentially derived from shale units in the hanging wall.

Section J3 in Figure 7 illustrates the geometry of folds when throw is small. In this case, the fold geometry has a smaller amplitude and wavelength and is monoclinical. The faults that cut sandstone do not appear to penetrate overlying shale units. Furthermore,



- shale derived from the Cutler Formation
- limestone of the Honaker Trail Formation
- sandstone derived from the Cutler Formation
- faults
- bedding



- shale
- sandstone
- faults
- bedding

the faults are located beneath the upper fold hinge on the footwall side of the monocline (e.g., section J2 in Figure 7), placing most of the fold on the hanging-wall side. This example illustrates the tendency for overlying shale units to fold instead of fault; thus, overlying shale units remain continuous across the fault.

Close to the fault, the units involved in folding typically kink sharply to a steeper dip angle, becoming subparallel to the fault slip surface (e.g., sections D, H, K, M, N, and S in Figure 7). This geometry is similar to the detailed cases (Figures 5, 6) where rotation, extension, and attenuation of beds are greatest in a narrow zone adjacent to the fault slip surface (which constitutes the fault core). As the distance from the kink point along the fault core increases, the thickness of the shale in the fault core slowly decreases. The result in these locations is a thin shale smear along the fault despite its proximity to a source of shale. In a small number of other locations, the broader scale folding locally and abruptly dies out over short distances (e.g., stations U and V in Figure 7). This geometric variation produces corresponding variations in the thickness of shale fault rocks along fault strike that are greatest close to the source of the shale in the hanging wall. However, in all of our examples, the kinked part of the fold is present and includes some shale separating sandstone in the footwall from sandstone in the hanging wall.

QUANTITATIVE MEASUREMENTS OF SHALE FAULT ROCK THICKNESS AND CONTROLLING PARAMETERS

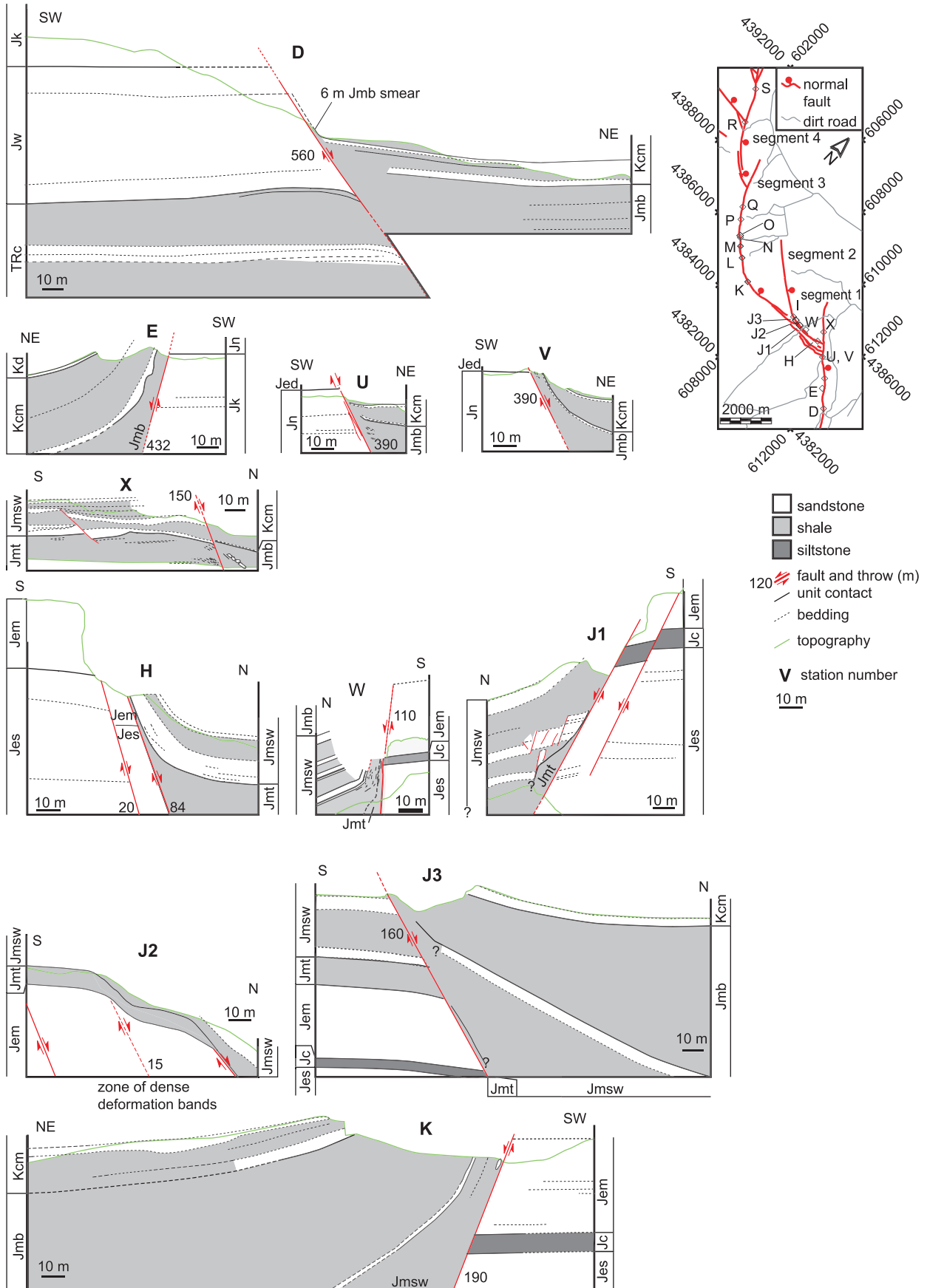
We interpret the consistency of the shale geometry in the fault zone (Figures 5–7) to suggest that a systematic process, consistent with the conceptual model in Figure 4c, governs the thickness distribution and persistence of shale in the fault zone. Evidence from the detailed maps of the fault zone indicates that several parameters might impact the distribution of shale fault rocks. In Figures 5–7, multiple shale layers combine to form the shale smear in the fault core. This suggests that the thickness of the shale fault rock might be related to the thickness of shale available in the stratigraphic

column. Similarly, the relative thickness of sandstone and shale units also appears to affect the shape of folding related to entrainment of the shale in the fault zone (e.g., Figure 6d). Furthermore, the thickness of shale fault rock consistently thins along the fault core away from the source of shale (Figures 5, 6d, 7). This geometry implies that both distance from the source of shale and, consequently, fault throw impact the distribution of shale fault rock. These two parameters are also practical in the field, because exposure is commonly limited, and therefore, it is not always possible to observe shale fault rocks at their thinnest point.

The stratigraphic distribution and relative thickness of sandstone and shale units are associated with two distinct types of fault architecture in the field examples. The first type occurs when shale layers are confined between thick, stiff sandstone layers that fold very little adjacent to the fault core (e.g., Figures 5, 6c) and is idealized in Figure 8a. The second type occurs when a thick sandstone layer is overlain by a shale-dominated sequence with a broad fold in the hanging wall (e.g., Figure 7) and is idealized in Figure 8b. In both cases, bedding in the shale is nearly parallel to the fault slip surfaces in the fault core. The first type is found where sandstone beds are typically as thick or thicker than shale beds (e.g., Curtis, Moenkopi, and Chinle formations and some small faults confined in the Salt Wash Member). The second type is more prevalent, where shale from the Morrison and Cedar Mountain formations and the Mancos Shale sits atop the thick, Jurassic sandstone sequence. We have distinguished these two types because it is likely that they may have different effects on the architecture of the fault zone and the incorporation of shale into the fault core.

To investigate the potential relationship between (1) the original thickness of shale incorporated in the fault rock, (2) the distance from the source of shale along the fault core, and (3) the fault throw with the thickness of shale in the fault core, we estimated the thickness of shale in each stratigraphic unit (Table 1) and made 162 measurements of the remaining parameters at 80 stations along the fault (Table 2). Most data were available from the northwestern portion of the fault (Figure 9a), where exposure is best, and the second type of fault zone architecture is typical (Figure 8b). Because the relative thickness of sandstone and shale units impacts the geometry of the shale smear (e.g.,

FIGURE 6. (a) Outcrop photo and (b) detailed cross section of deformed interbedded sandstone and shale derived from the Cutler Formation juxtaposed against limestone from the Honaker Trail Formation near the entrance to Arches National Park. Sandstone beds are faulted and extended, whereas shale beds have thinned but remain continuous. This outcrop is located at 62°00'86"E, 42°74'72.5"N (Zone 12N, NAD27). Throw on this segment of the Moab fault is approximately 250 m (820 ft). (c) Outcrop photo and (d) simplified cross section of two fault strands located at 61°76'67"E, 42°76'78.9"N (Zone 12N, NAD27). Combined throw across both segments is about 906 m (2970 ft). (e) Detailed photo of (c) and (d) depicting entrainment of sandstone blocks and breccia in shale.



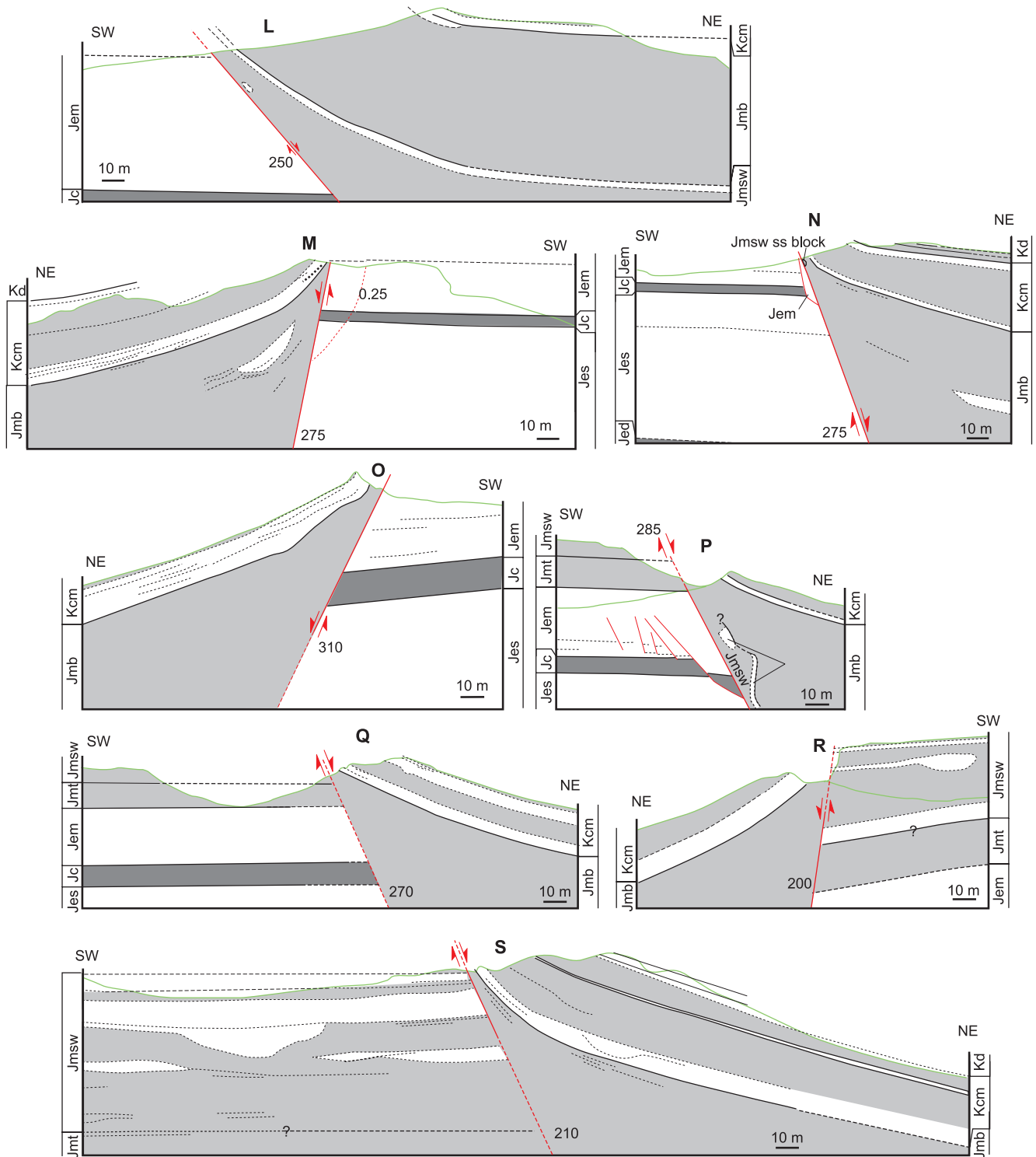


FIGURE 7. Cross sections of fault exposures along the northwestern portion of the Moab fault system. Section locations and letter designations are shown in an index map but, in general, are ordered from east to west. Downdip exposure at the selected locations allowed us to document the geometry of shale units as they approach the fault zone. Cross sections are limited to directly observable features, are not extrapolated into the subsurface, and do not show the detailed structure in damage zones. Note that abbreviations of stratigraphic names are defined in Figure 2.

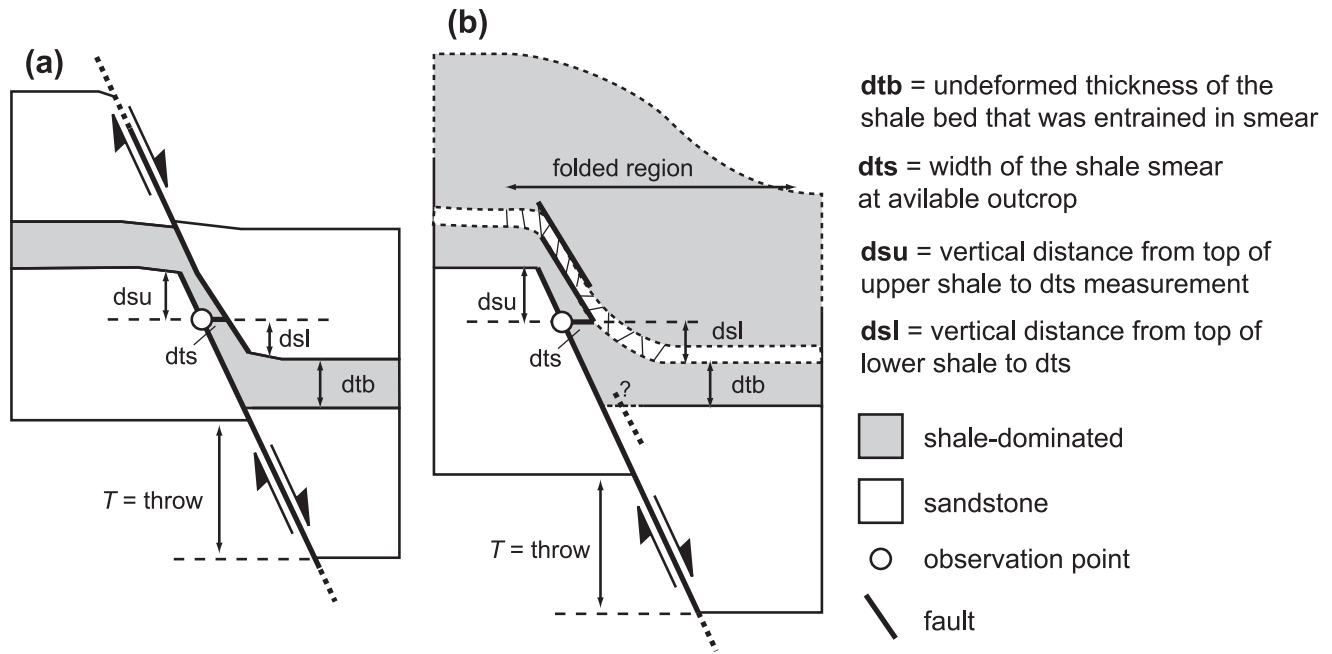


FIGURE 8. Schemes for quantifying the change in (or distribution of) shale smear width related to: throw, thickness of and distance from the source bed of shale, fault geometry, and geometry of stratigraphy. (a) Typical shale smear model (e.g., Aydin and Eyal, 2002) consisting of a compliant unit sandwiched between two stiffer units. (b) A two-layer system with thick sandstone below and dominantly shale above.

Figure 8), we have only plotted data from examples corresponding to case 2 in Figure 9.

For convenience in the field, we measured the width of shale fault rock along a horizontal line from the fault slip surface to the identifiable top of any shale-dominated stratigraphic unit. The location of this measurement was determined by outcrop availability. For each measurement of the width of the shale fault rock (dts in Figure 8), we also determined a distance from the nearest potential source of shale in the hanging wall. This distance (dsl in Figure 8) was measured by projecting the top of the stratigraphic unit from the nearest location where the unit lies at the regional strike and dip into the fault core. Finally, we estimated the total thickness of shale units that could have contributed to the shale fault rock (dtb in Figure 8) based on the measured stra-

tigraphy, fault throw, and the units juxtaposed at the observation point.

The distribution of smeared shale width has a consistent shape (Figure 9b, c) for individual examples of shale smear. In each case, the width of the smeared shale decreases monotonically with increasing distance from the hanging-wall source of the shale (dsl) and defines a continuous shale smear. These curves have a generally asymptotic shape, indicating that thin shale smears (a few meters thick) persist for long distances in the fault core with only a slight tapering in thickness. The width of the smeared shale reaches a minimum as the distance from the hanging-wall source of shale approaches the throw (T). This might imply that shale in these smears is primarily derived from units in the hanging wall instead of the footwall.

Table 1. Potential shale sources estimated from field observation and data from Doelling (1982, 1988).

Stratigraphic Unit (See Figure 2)	Thickness (dtb) (m)	Total shale (m)	Error (m; \pm)
Jmb	80	90	10
Jmsw	68	50	15
Jmt	20	20	5
Trc	110	70	15
TRm	125	70	35
Pc	320	120	50

However, a simple relationship that relates the change in width of the smear to throw or distance from sources of shale is not evident (Figure 9d). In each case, some shale fault rock is present in the fault zone, which is consistent with the nearly asymptotic curve defining the rate of change in the width of the shale smear observed in Figure 9b and c. However, when comparing examples from different parts of the fault, a great deal of heterogeneity exists. The major distinction appears to be the ratio of dts/T that marks the transition from rapid thinning in the smear to a slow rate of thinning with increasing dts/T , which is different for many of the examples (Figure 9b, c). In some cases, this heterogeneity is associated with complications in the fault geometry or the shape of the fold in the hanging wall. For instance, segmentation of the fault system along strike appears to be a factor in maintaining larger smear widths (e.g., Figure 6d and section J2 in Figure 7). In these cases, the segmentation distributes the throw among several faults with smaller throw. Consequently, each fault segment has a relatively wide smear. In other cases where a narrow fold hinge exists in the hanging wall, the value of dts may be very low for all ratios of dts/T . As a result, thin shale smears can occur at small throw.

We do find that shale from a given unit is absent from the fault zone where throw is beyond some maximum magnitude. The Tidwell Member (Jmt) vanishes when throw is about 150 m (490 ft) (T/dtb is larger than 7.5–8 in Figure 9), and the Salt Wash Member disappears when throw is about 270 m (886 ft) (T/dtb is larger than 3.7–4). The Brushy Basin Member is never visibly attenuated to zero width, which includes examples with throw as much as 560 m (1840 ft) (T/dtb is larger than 3.5). As a result, these measurements provide an empirical criterion for estimating the maximum distance from shale beds that shale fault rocks might be distributed in the fault core.

DISTRIBUTION OF FAULT ZONE STRUCTURES IN THREE DIMENSIONS

The fault zone along the Moab fault system in Permian to Cretaceous sandstone and shale consists of structures from three distinct faulting mechanisms (Figures 10, 11). In sandstone from all stratigraphic units, deformation band-based structures occur everywhere along the Moab fault (Davatzes, 2003) and form a core and damage zone of variable width in sandstone units. In folded hanging-wall sandstone layers, deformation bands are also distributed throughout folds. Joint-based structures overprint deformation bands at locations with complex fault geometry, such as intersections

and relays along either strike or dip (Davatzes, 2003). In addition, joints occur in great density in all folded hanging-wall sandstone layers, again overprinting deformation bands.

Shale is incorporated into the fault zone over the area between a shale unit's position in the footwall and its corresponding position in the hanging wall (idealized in Figure 8). Individual shale units smeared in the fault core taper to zero at large throw. Broad folds in the hanging wall define wide damage zones in shale-dominated units that are absent in the footwall. Folds or faults in sandstone along the contact between the thick Jurassic sandstone package and overlying shale might be necessary to conserve the volume of smeared and folded shale in the hanging wall but are commonly poorly exposed. These kinds of folds and faults are evident in the relays in cross sections in Figure 11c and d and near the intersection in Figure 11b between segments 1 and 2.

We used data presented in this study, previously published data from the Moab fault (Foxford et al., 1998; Doelling, 2002; Davatzes, 2003; Davatzes and Aydin, 2003), and criteria for characterizing the distribution of fault zone structures (Davatzes, 2003) and smear thickness to map fault architecture onto juxtaposition diagrams (Allan, 1989; Knipe, 1997), thus representing the three-dimensional architecture of the Moab fault system. The fault plane geometry and juxtaposition diagrams were constructed using publicly available well data from the Utah Division of Oil, Gas, and Mining, published cross sections (Doelling, 1988; Doelling, 2002), detailed stratigraphic sections (Doelling, 1982), mapped formation contacts (Figure 3), a 10-m (33-ft) resolution digital elevation model, and measured strikes and dips of bedding. Additional cross sections both normal and parallel to the fault were constructed to constrain stratigraphic horizons produced in GoCAD®. The initial juxtaposition diagram was then constructed using Fault Analysis Projection System (FAPS®). GoCAD and FAPS are commercially available software used for three-dimensional reservoir model construction and fault plane analysis, respectively.

Traditional juxtaposition (also called Allan) diagrams plot the distribution of rock types that intersect and are juxtaposed across an idealized fault plane (Allan, 1989; Knipe, 1997). This analysis typically assumes that the fault zone itself has no impact on sealing and is a plane of zero thickness. We have used the distribution of lithologic units from the juxtaposition analysis as a first-order control on the distribution of fault zone structures. The resulting diagram is broken into three sets: (1) footwall damage zone immediately adjacent to the fault core (Figure 12a); (2) hanging-wall damage zone immediately adjacent to the fault core (Figure 12b); and (3) fault core (Figure 12c). The plane or map that represents each portion of the fault zone (damage zones

Table 2. Quantitative shale-shear data and potential controlling parameters. Easting and northing are expressed as UTM coordinates, Zone 12N, NAD27. Note that abbreviations of stratigraphic names are defined in Figure 2.

<i>Station</i>	<i>Segment</i>	<i>Easting (m)</i>	<i>Northing (m)</i>	<i>Elevation (Meters above Sea Level)</i>	<i>Throw (m)</i>	<i>Estimated Elevation of Shale Source Unit Top</i>	<i>dsl (m)</i>	<i>dsu (m)</i>	<i>Unit in Footwall</i>	<i>Unit in Hanging Wall</i>	<i>Potential Sources of Shale</i>	<i>dts (m)</i>	<i>dsl/T</i>	<i>dts/ dtb</i>
S1	4	601628	4290451	-	210	-	150	60	Jmsw bottom third	Jmb top	Jm	8.0	0.71	0.05
S3	4	601628	4290451	-	210	-	145	65	Jmsw bottom third	Jmb top	Jm	15.0	0.69	0.09
S4	4	601628	4290451	-	210	-	140	70	Jmsw bottom third	Jmb top	Jm	16.0	0.67	0.10
S5	4	601628	4290451	-	210	-	135	75	Jmsw bottom third	Jmb top	Jm	19.0	0.64	0.12
S6	4	601628	4290451	-	210	-	130	80	Jmsw bottom third	Jmb top	Jm	21.0	0.62	0.13
S7	4	601628	4290451	-	210	-	125	85	Jmsw bottom third	Jmb top	Jm	24.0	0.60	0.15
S8	4	601628	4290451	-	210	-	120	90	Jmsw bottom third	Jmb top	Jm	29.0	0.57	0.18
S9	4	601628	4290451	-	210	-	115	95	Jmsw bottom third	Jmb top	Jm	36.0	0.55	0.23
S10	4	601628	4290451	-	210	-	110	100	Jmsw bottom third	Jmb top	Jm	46.0	0.52	0.29
S11	4	601628	4290451	-	210	-	105	105	Jmsw bottom third	Jmb top	Jm	61.0	0.50	0.38
S12	4	601628	4290451	-	210	-	100	110	Jmsw bottom third	Jmb top	Jm	70.0	0.48	0.44
S13	4	601628	4290451	-	210	-	95	115	Jmsw bottom third	Jmb top	Jm	89.0	0.45	0.56
S14	4	601628	4290451	-	210	-	90	120	Jmsw bottom third	Jmb top	Jm	111.0	0.43	0.69
S15	4	601628	4290451	-	210	-	85	125	Jmsw bottom third	Jmb top	Jm	126.0	0.40	0.79
R1	4	602263	4288284	1463	200	1390	78	122	Jmsw bottom third	Kd bottom	Jm	3.0	0.39	0.03
R2	4	602263	4288284	1458	200	1390	73	127	Jmsw bottom third	Kd bottom	Jm	10.0	0.37	0.08
R3	4	602263	4288284	1453	200	1390	68	132	Jmsw bottom third	Kd bottom	Jm	14.0	0.34	0.12
R4	4	602263	4288284	1448	200	1390	63	137	Jmsw bottom third	Kd bottom	Jm	18.0	0.32	0.15
R5	4	602263	4288284	1443	200	1390	58	142	Jmsw bottom third	Kd bottom	Jm	25.0	0.29	0.21
R6	4	602263	4288284	1438	200	1390	53	147	Jmsw bottom third	Kd bottom	Jm	32.0	0.27	0.27
R7	4	602263	4288284	1433	200	1390	48	152	Jmsw bottom third	Kd bottom	Jm	39.0	0.24	0.33
R8	4	602263	4288284	1428	200	1390	43	157	Jmsw bottom third	Kd bottom	Jm	48.0	0.22	0.40
R9	4	602263	4288284	1423	200	1390	38	162	Jmsw bottom third	Kd bottom	Jm	57.0	0.19	0.48
R10	4	602263	4288284	1418	200	1390	33	167	Jmsw bottom third	Kd bottom	Jm	68.0	0.17	0.57
R11	4	602263	4288284	1413	200	1390	28	172	Jmsw bottom third	Kd bottom	Jm	72.0	0.14	0.60
Q1	3	604533	4286836	1472	270	1435	37	233	Jem top	Jmb top third	Jm	7.0	0.14	0.05
Q2	3	604533	4286836	1467	270	1435	32	238	Jem top	Jmb top third	Jm	17.0	0.12	0.12
Q3	3	604533	4286836	1462	270	1435	27	243	Jem top	Jmb top third	Jm	25.0	0.10	0.18
Q4	3	604533	4286836	1457	270	1435	22	248	Jem top	Jmb top third	Jm	35.0	0.08	0.25
Q1	3	604533	4286836	1452	270	1435	17	253	Jem top	Jmb top third	Jm	45.0	0.06	0.32
Q2	3	604533	4286836	1447	270	1435	12	258	Jem top	Jmb top third	Jm	60.0	0.04	0.43
Q3	3	604533	4286836	1442	270	1435	7	263	Jem top	Jmb top third	Jm	73.0	0.03	0.52
1	3	604533	4286836	1468	280	1426	42	238	Jem	Jmb	Jm	4.0	0.15	0.03
3	3	604830	4286433	1461	285	1426	35	250	Jes	Jmb top	Jm	5.6	0.12	0.04

Table 2. Quantitative shale-shear data and potential controlling parameters. Easting and northing are expressed as UTM coordinates, Zone 12N, NAD27. Note that abbreviations of stratigraphic names are defined in Figure 2 (cont.).

<i>Station</i>	<i>Segment</i>	<i>Easting (m)</i>	<i>Northing (m)</i>	<i>Elevation (Meters above Sea Level)</i>	<i>Throw (m)</i>	<i>Estimated Elevation of Shale Source Unit Top</i>	<i>dsl (m)</i>	<i>dsu (m)</i>	<i>Unit in Footwall</i>	<i>Unit in Hanging Wall</i>	<i>Potential Sources of Shale</i>	<i>dts (m)</i>	<i>dsl/T</i>	<i>dts/ dtb</i>
P1	3	604830	4286433	1450	285	1430	25	260	Jes	Jmb top	Jm	16.0	0.09	0.10
P2	3	604830	4286433	1445	285	1430	20	265	Jes	Jmb top	Jm	25.0	0.07	0.16
P3	3	604830	4286433	1440	285	1430	15	270	Jes	Jmb top	Jm	35.0	0.05	0.22
P4	3	604830	4286433	1435	285	1430	10	275	Jes	Jmb top	Jm	47.0	0.04	0.29
P5	3	604830	4286433	1430	285	1430	5	280	Jes	Jmb top	Jm	60.0	0.02	0.38
4	3	605286	4285922	1433	285	1425	8	277	Jem top	Kcm	Jm	3.5	0.03	0.02
5	3	605318	4285916	1485	280	1425	60	220	Jem bottom	Jmb top	Jm	11.0	0.21	0.07
O1	3	605318	4285916	1468	310	1417	51	259	Jem mid	Jmsw top	Jmsw + Jmt	7.0	0.16	0.10
O2	3	605318	4285916	1463	310	1417	46	264	Jem mid	Jmsw top	Jmsw + Jmt	10.0	0.15	0.14
O3	3	605318	4285916	1458	310	1417	41	269	Jem mid	Jmsw top	Jmsw + Jmt	17.0	0.13	0.24
O4	3	605318	4285916	1453	310	1417	36	274	Jem mid	Jmsw top	Jmsw + Jmt	21.0	0.12	0.30
O5	3	605318	4285916	1448	310	1417	31	279	Jem mid	Jmsw top	Jmsw + Jmt	24.0	0.10	0.34
O6	3	605318	4285916	1443	310	1417	26	284	Jem mid	Jmsw top	Jmsw + Jmt	27.0	0.08	0.39
O7	3	605318	4285916	1438	310	1417	21	289	Jem mid	Jmsw top	Jmsw + Jmt	38.0	0.07	0.54
O8	3	605318	4285916	1433	310	1417	16	294	Jem mid	Jmsw top	Jmsw + Jmt	50.0	0.05	0.71
O9	3	605318	4285916	1428	310	1417	11	299	Jem mid	Jmsw top	Jmsw + Jmt	60.0	0.04	0.86
O10	3	605318	4285916	1423	310	1417	6	304	Jem mid	Jmsw top	Jmsw + Jmt	72.0	0.02	1.03
O11	3	605318	4285916	1418	310	1417	1	309	Jem mid	Jmsw top	Jmsw + Jmt	84.0	0.00	1.20
O12	3	605318	4285916	1413	310	1417	-4	314	Jem mid	Jmsw top	Jmsw + Jmt	96.0	-0.01	1.37
M1	3	605565	4285675	1486	275	1409	77	198	Jem top	Jmb top	Jm	2.0	0.28	0.01
M2	3	605565	4285675	1481	275	1409	72	203	Jem top	Jmb top	Jm	5.0	0.26	0.03
M3	3	605565	4285675	1476	275	1409	67	208	Jem top	Jmb top	Jm	7.0	0.24	0.04
M4	3	605565	4285675	1471	275	1409	62	213	Jem top	Jmb top	Jm	12.0	0.23	0.08
M5	3	605565	4285675	1466	275	1409	57	218	Jem top	Jmb top	Jm	17.0	0.21	0.11
M6	3	605565	4285675	1461	275	1409	52	223	Jem top	Jmb top	Jm	27.0	0.19	0.17
M7	3	605565	4285675	1456	275	1409	47	228	Jem top	Jmb top	Jm	40.0	0.17	0.25
M8	3	605565	4285675	1451	275	1409	42	233	Jem top	Jmb top	Jm	53.0	0.15	0.33
M9	3	605565	4285675	1446	275	1409	37	238	Jem top	Jmb top	Jm	68.0	0.13	0.43
M10	3	605565	4285675	1441	275	1409	32	243	Jem top	Jmb top	Jm	88.0	0.12	0.55
M11	3	605565	4285675	1436	275	1409	27	248	Jem top	Jmb top	Jm	95.0	0.10	0.59
M12	3	605565	4285675	1431	275	1409	22	253	Jem top	Jmb top	Jm	140.0	0.08	0.88
N1	3	605565	4285675	1476	275	1409	67	208	Jes top	Jmb top	Jm	3.0	0.24	0.02
N2	3	605565	4285675	1471	275	1409	62	213	Jes top	Jmb top	Jm	4.0	0.23	0.03

Table 2. Quantitative shale-smear data and potential controlling parameters. Easting and northing are expressed as UTM coordinates, Zone 12N, NAD27. Note that abbreviations of stratigraphic names are defined in Figure 2 (cont.).

<i>Station</i>	<i>Segment</i>	<i>Easting (m)</i>	<i>Northing (m)</i>	<i>Elevation (Meters above Sea Level)</i>	<i>Throw (m)</i>	<i>Estimated Elevation of Shale Source Unit Top</i>	<i>dsl (m)</i>	<i>dsu (m)</i>	<i>Unit in Footwall</i>	<i>Unit in Hanging Wall</i>	<i>Potential Sources of Shale</i>	<i>dts (m)</i>	<i>dsl/T</i>	<i>dts/ dtb</i>
N3	3	605565	4285675	1466	275	1409	57	218	Jes top	Jmb top	Jm	9.0	0.21	0.06
N4	3	605565	4285675	1461	275	1409	52	223	Jes top	Jmb top	Jm	19.0	0.19	0.12
N5	3	605565	4285675	1456	275	1409	47	228	Jes top	Jmb top	Jm	33.0	0.17	0.21
N6	3	605565	4285675	1451	275	1409	42	233	Jes top	Jmb top	Jm	47.0	0.15	0.29
N7	3	605565	4285675	1446	275	1409	37	238	Jes top	Jmb top	Jm	63.0	0.13	0.39
N8	3	605565	4285675	1441	275	1409	32	243	Jes top	Jmb top	Jm	84.0	0.12	0.53
L1	3	605930	4285400	1476	250	1410	66	184	Jem top	Jmsw top	Jm	30.0	0.26	0.19
L2	3	605930	4285400	1476	250	1320	156	94	Jem top		Jmsw + Jmt	10.0	0.62	0.06
L3	3	605930	4285400	1471	250	1320	151	99	Jem top		Jmsw + Jmt	12.0	0.60	0.08
L4	3	605930	4285400	1466	250	1320	146	104	Jem top		Jmsw + Jmt	13.0	0.58	0.08
L5	3	605930	4285400	1461	250	1320	141	109	Jem top		Jmsw + Jmt	16.0	0.56	0.10
L6	3	605930	4285400	1456	250	1320	136	114	Jem top		Jmsw + Jmt	19.0	0.54	0.12
L7	3	605930	4285400	1451	250	1320	131	119	Jem top		Jmsw + Jmt	22.0	0.52	0.14
L8	3	605930	4285400	1446	250	1320	126	124	Jem top		Jmsw + Jmt	27.0	0.50	0.17
L9	3	605930	4285400	1441	250	1320	121	129	Jem top		Jmsw + Jmt	34.0	0.48	0.21
L10	3	605930	4285400	1436	250	1320	116	134	Jem top		Jmsw + Jmt	40.0	0.46	0.25
L11	3	605930	4285400	1431	250	1320	111	139	Jem top		Jmsw + Jmt	48.0	0.44	0.30
L12	3	605930	4285400	1426	250	1320	106	144	Jem top		Jmsw + Jmt	57.0	0.42	0.36
L13	3	605930	4285400	1421	250	1320	101	149	Jem top		Jmsw + Jmt	80.0	0.40	0.50
L14	3	605930	4285400	1416	250	1320	96	154	Jem top		Jmsw + Jmt	160.0	0.38	1.00
K1	3	606746	4284891	1486	190	1360	126	64	Jem top	Jmb top	Jmsw + Jmt	14.0	0.66	0.20
K2	3	606746	4284891	1481	190	1360	121	69	Jem top	Jmb top	Jmsw + Jmt	13.0	0.64	0.19
K3	3	606746	4284891	1476	190	1360	116	74	Jem top	Jmb top	Jmsw + Jmt	14.0	0.61	0.20
K4	3	606746	4284891	1471	190	1360	111	79	Jem top	Jmb top	Jmsw + Jmt	15.0	0.58	0.21
K5	3	606746	4284891	1466	190	1360	106	84	Jem top	Jmb top	Jmsw + Jmt	17.0	0.56	0.24
K6	3	606746	4284891	1461	190	1360	101	89	Jem top	Jmb top	Jmsw + Jmt	20.0	0.53	0.29
K7	3	606746	4284891	1456	190	1360	96	94	Jem top	Jmb top	Jmsw + Jmt	24.0	0.51	0.34
K8	3	606746	4284891	1451	190	1360	91	99	Jem top	Jmb top	Jmsw + Jmt	27.0	0.48	0.39
K9	3	606746	4284891	1446	190	1360	86	104	Jem top	Jmb top	Jmsw + Jmt	32.0	0.45	0.46
K10	3	606746	4284891	1441	190	1360	81	109	Jem top	Jmb top	Jmsw + Jmt	38.0	0.43	0.54
K2	3	606746	4284891	1486	190	1450	36	154	Jem top	Jmsw top	Jm	50.0	0.19	0.31
13	3	607565	4284847	1484	115	1411	73	42	Jem top	Jmsw top	Jmsw + Jmt	2.0	0.63	0.03
14	3	607633	4284869	1462	110	1416	46	64	Jem top	Jmsw top	Jmsw + Jmt	6.5	0.42	0.09
15	3	607670	4284885	1448	110	1416	32	78	Jem bottom	Jmsw top	Jmsw + Jmt	5.1	0.29	0.10

Table 2. Quantitative shale-smear data and potential controlling parameters. Easting and northing are expressed as UTM coordinates, Zone 12N, NAD27. Note that abbreviations of stratigraphic names are defined in Figure 2 (cont.).

Station	Segment	Easting (m)	Northing (m)	Elevation (Meters above Sea Level)	Throw (m)	Estimated Elevation of Shale Source Unit Top	dsl (m)	dsu (m)	Unit in Footwall	Unit in Hanging Wall	Potential Sources of Shale	dts (m)	dsl/T	dts/ dtb
16	3	607968	4284929	1440	95	1416	24	71	Curtis	Jmsw bottom	Jmt	2.0	0.25	0.10
17	3	608122	4284922	1443	90	1416	27	63	Curtis	Jmsw bottom	Jmt	7.0	0.30	0.14
18	3	608483	4284938	1450	85	1420	30	55	Jem top	Jmsw bottom	Jmt	8.0	0.35	0.11
19	3	608732	4284945	1474	60	1440	34	26	Jem top	Jmsw bottom	Jmt	7.8	0.57	0.16
	2	608990	4285190	1464	155	1411	53	102	Jem top	Jmb/Kcm	Jm	76.0	0.34	0.48
20	2	609306	4285136	1415	115	1310	105	10	Jem top	Jmsw bottom	Jmsw + Jmt	4.1	0.91	0.21
21	2	609348	4285139	1410	110	1310	100	10	Jem bottom	Jmsw bottom	Jmt	3.0	0.91	0.15
23	2	609488	4285117	1390	110	1330	60	50	Jes top	Jmsw bottom	Jmsw/Jmt	2.7	0.55	0.05
24	2	609574	4285099	1395	140	1330	65	75	Jes top	Jem bottom	Jmsw/Jmt	0.3	0.46	0.01
25a	2	609607	4285091	1420	140	1319	101	39	Jes top	Jmsw bottom	Jmt	0.7	0.72	0.04
25b	2	609607	4285091	1420	140	1379	41	99	Jes top	Jmsw mid	Jmt + Jmsw part	7.0	0.29	0.18
T	2	609684	4285176	-	1	-	0.1	0.1	Jmsw	Jmsw	Jmsw internal	0.1	0.10	0.05
26	2	609696	4285108	1417	130	1379	38	92	Jes	Jmsw top	Jmt	10.0	0.29	0.15
28	2	609789	4285108	1415	125	1380	35	90	Jes	Jmsw bottom	Jmt	4.0	0.28	0.08
29	2	609906	4285066	1440	120	1380	60	60	Jes top	Jmsw bottom	Jmt + Jmsw part	5.0	0.50	0.10
30	2	610283	4285152	1415	95	1380	35	60	Jem top	Jmsw bottom	Jmt	1.8	0.37	0.09
31	2	610291	4285157	1408	95	1380	28	67	Jem top	Jmsw bottom	Jmt	1.5	0.29	0.08
32	2	610302	4285167	1402	90	1380	22	68	Jem top	Jmsw bottom	Jmt	0.8	0.24	0.04
H1	2	610324	4285185	1410	84	1380	30	54	Jes top	Jmt top	Jmt	0.8	0.36	0.04
H2	2	610324	4285185	1405	84	1380	25	59	Jes top	Jmt top	Jmt	1.0	0.30	0.05
H3	2	610324	4285185	1400	84	1380	20	64	Jes top	Jmt top	Jmt	1.2	0.24	0.06
H4	2	610324	4285185	1395	84	1380	15	69	Jes top	Jmt top	Jmt	1.0	0.18	0.05
H5	2	610324	4285185	1390	84	1380	10	74	Jes top	Jmt top	Jmt	2.0	0.12	0.10
H6	2	610324	4285185	1385	84	1380	5	79	Jes top	Jmt top	Jmt	4.0	0.06	0.20
H7	2	610324	4285185	1380	84	1380	0	84	Jes top	Jmt top	Jmt	7.0	0.00	0.35
H8	2	610324	4285185	1375	84	1380	-5	89	Jes top	Jmt top	Jmt	13.0	-0.06	0.65
H9	2	610324	4285185	1370	84	1380	-10	94	Jes top	Jmt top	Jmt	55.0	-0.12	2.75
G	1	610237	4285604	1381	150	1380	1	149	Jmt top	Kcm bottom	Jm	5.0	0.01	0.03
34	1	610435	4285392	1389	375	1379	10	90	Jem top	Jmb top	Jmt	3.0	0.03	0.15
36	1	610467	4285364	1397	85	1379	18	67	Jem top	Jmb top	Jmt	3.9	0.21	0.20
37	1	610501	4285341	1399	80	1379	20	60	Jem top	Jmb top	Jmt	1.0	0.25	0.05
39	1	610521	4285328	1398	290	1379	19	271	Jem top	Jmb top	Jmt	2.5	0.07	0.13
40	1	610569	4285287	1400	300	1379	21	279	Jem bottom	Jmb top	Jmt	1.6	0.07	0.08
41	1	610638	4285205	1407	335	1379	28	307	Jes bottom	Jmb top	Jmt	3.0	0.08	0.15

Table 2. Quantitative shale-smear data and potential controlling parameters. Easting and northing are expressed as UTM coordinates, Zone 12N, NAD27. Note that abbreviations of stratigraphic names are defined in Figure 2 (cont.).

<i>Station</i>	<i>Segment</i>	<i>Easting (m)</i>	<i>Northing (m)</i>	<i>Elevation (Meters above Sea Level)</i>	<i>Throw (m)</i>	<i>Estimated Elevation of Shale Source Unit Top</i>	<i>dsl (m)</i>	<i>dsu (m)</i>	<i>Unit in Footwall</i>	<i>Unit in Hanging Wall</i>	<i>Potential Sources of Shale</i>	<i>dts (m)</i>	<i>dsl/T</i>	<i>dts/ dtb</i>
42	1	610645	4285197	1402	340	1379	23	317	Jes top	Jmb top	Jmt	2.9	0.07	0.15
43	1	610880	4284905	1432	385	1396	36	349	Jn bottom	Kcm bottom	Jm	5.6	0.09	0.04
U	1	610895	4284883	1428	390	1394	34	356	Jn top	Kcm	Jm	5.0	0.09	0.03
V	1	610910	4284860	1429	390	1394	35	355	Jn top	Kcm	Jm	2.8	0.09	0.02
44	1	610973	4284802	1433	390	1396	37	353	Jn top	Kcm bottom	Jm	1.5	0.09	0.01
45	1	611000	4284771	1433	390	1396	37	353	Jn top	Kcm bottom	Jm	2.3	0.09	0.01
46	1	611067	4284712	1426	395	1396	30	365	Jn top	Kcm bottom	Jm	0.2	0.08	0.00
47	1	611108	4284701	1416	405	1398	18	387	Jn top	Kcm bottom	Jm	0.3	0.04	0.00
48	1	611199	4284628	1453	420	1398	55	365	Jn top	Kcm bottom	Jm	3.3	0.13	0.02
49	1	611293	4284560	1460	430	1400	60	370	Jn top	Kcm bottom	Jm	2.6	0.14	0.02
50	1	611376	4284492	1462	445	1400	62	383	Jn top	Kcm bottom	Jm	5.6	0.14	0.04
51	1	611481	4284432	1437	460	1400	37	423	Jk top	Kcm	Jm	2.0	0.08	0.01
E1	1	611550	4284350	1451	432	1400	51	381	Jk top	Jmb top	Jm	5.6	0.12	0.04
E2	1	611550	4284350	1446	432	1400	46	386	Jk top	Jmb top	Jm	5.0	0.11	0.03
E3	1	611550	4284350	1441	432	1400	41	391	Jk top	Jmb top	Jm	7.0	0.09	0.04
E4	1	611550	4284350	1436	432	1400	36	396	Jk top	Jmb top	Jm	7.0	0.08	0.04
E5	1	611550	4284350	1431	432	1400	31	401	Jk top	Jmb top	Jm	8.0	0.07	0.05
E6	1	611550	4284350	1426	432	1400	26	406	Jk top	Jmb top	Jm	12.0	0.06	0.08
E7	1	611550	4284350	1421	432	1400	21	411	Jk top	Jmb top	Jm	16.0	0.05	0.10
E8	1	611550	4284350	1416	432	1400	16	416	Jk top	Jmb top	Jm	23.0	0.04	0.14
	1	611760	4284010	1450	520	1414	36	484	Jk, 30 m below top	Kcm bot	Jm	8.0	0.07	0.05
D	1	612350	4283480	1472	560	1383	89	471	Jw bottom	Kd	Jm	6.0	0.16	0.04
C1	1	617667	4276789	1382	60	–	55	5	Jem	Jmsw bottom	Jmt	3.0	0.92	0.15
C2	1	617667	4276789	1382	880	–	?	?	Pc bottom	Jem	TRc + TRm + Jmt + Jmsw	3.0	?	0.00
C3	1	617637	4276798	1382	940		?	?	Pc bottom	Jmsw	TRc + TRm + Jmt + Jmsw	4.0	?	0.00
B	1	618661	4275392	1290	912		?	?	Pc	Jmsw bottom	Jmt	3.0	?	0.15
A	1	620086	4274725	1282	250		?	?	Pht top	Pc	Pc/Pht	4.0	?	0.02

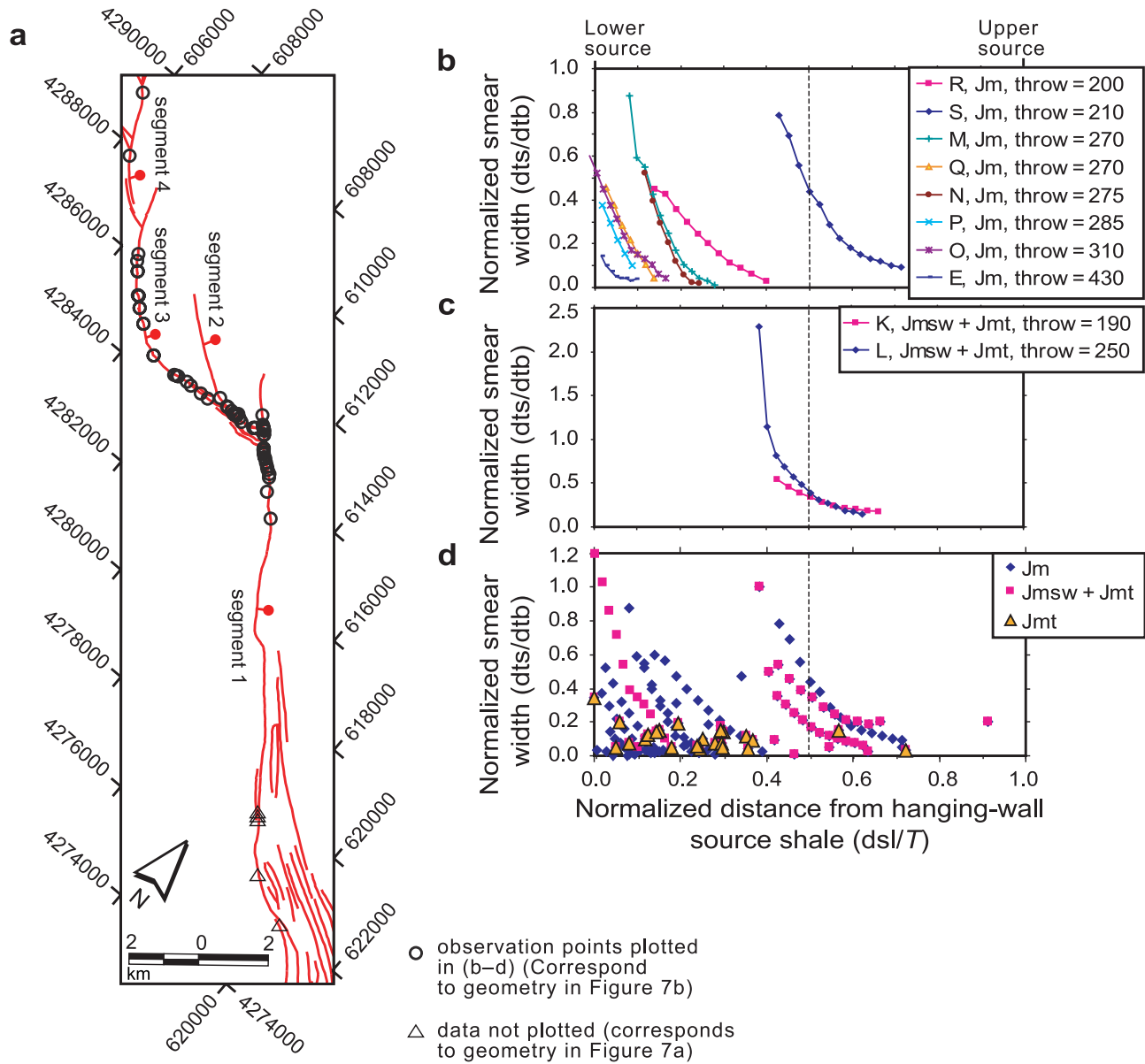


FIGURE 9. (a) Index map indicating locations of measurements. Variation of shale smear width vs. the distance from the source of shale in the hanging wall (dsl) normalized by the throw for shale derived from (b) the Brushy Basin Member, (c) the Salt Wash Member, and (d) for all units in the Morrison Formation. Smear width in (b–d) is normalized to the thickness of the inferred source of shale to facilitate comparisons between different observation points. Note that abbreviations of stratigraphic names are defined in Figure 2.

and core) maps the presence or absence of fault zone structures.

The architecture of the damage zones is largely dependent on the rock type in which they occur. The architecture of the fault core at any point is affected by any unit faulted past that position. Thus, the fault core at a point on the diagram might contain smeared shale even if shale is not currently juxtaposed against that point. Consequently, distinguishing the fault cores from the damage zone provides a means of recognizing where

these different parts of the fault zone might have different hydraulic properties. The fault core of most segments is dominated by shale-related fault rocks derived from either the Pennsylvanian to Triassic section or the Late Jurassic to Cretaceous section. Fault segments through the Jurassic sandstone section are composite zones of deformation bands, with locally developed breccia zones, and shale gouge resulting from offset of units rich in shale. In most locations, the fault is a composite of structures resulting from different faulting mechanisms.

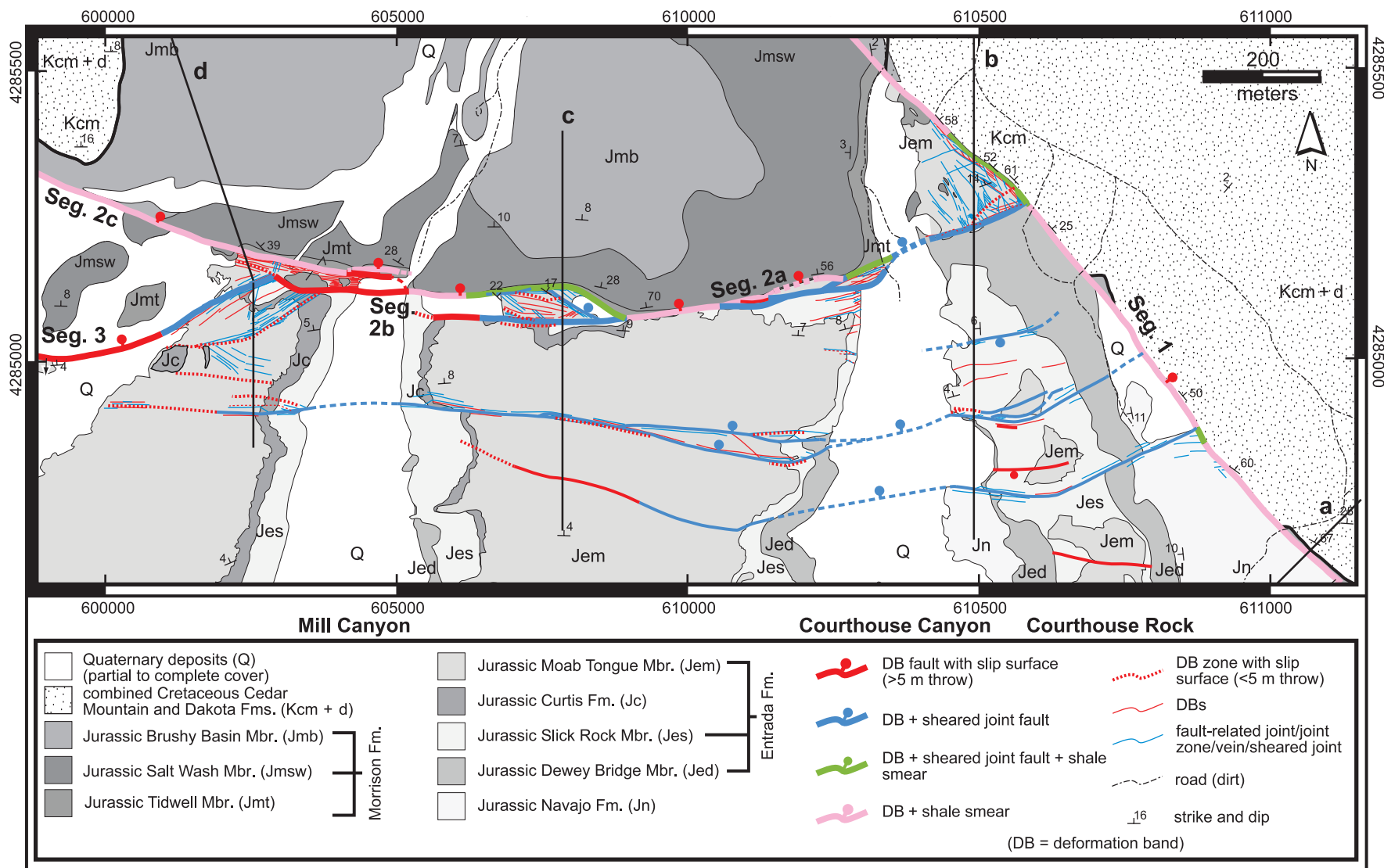


FIGURE 10. Map of the distribution of different types of fault zone structures resulting from distinct faulting mechanisms observed in sandstone and shale along a portion of the Moab fault. Locations of cross sections in Figure 11 are indicated.

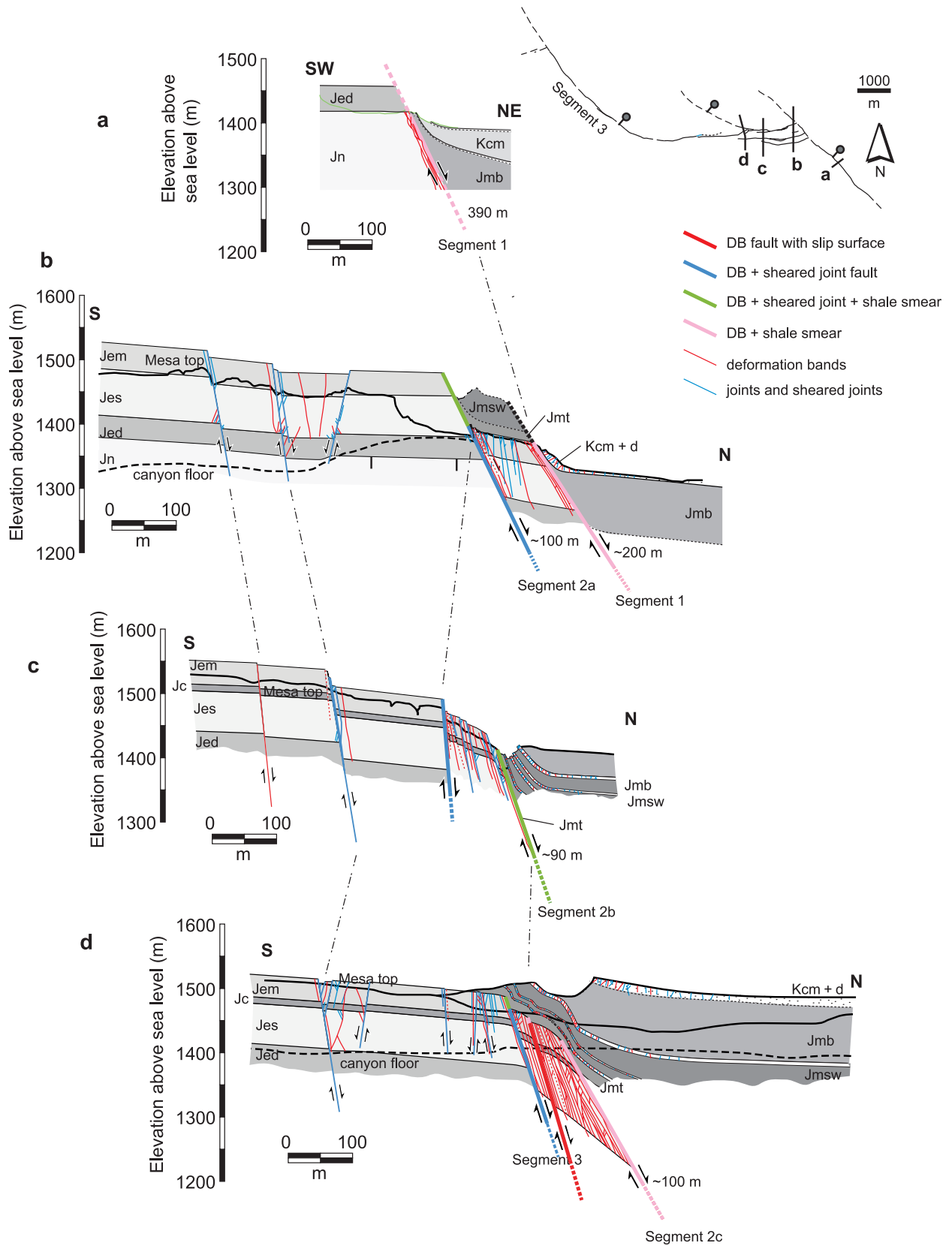
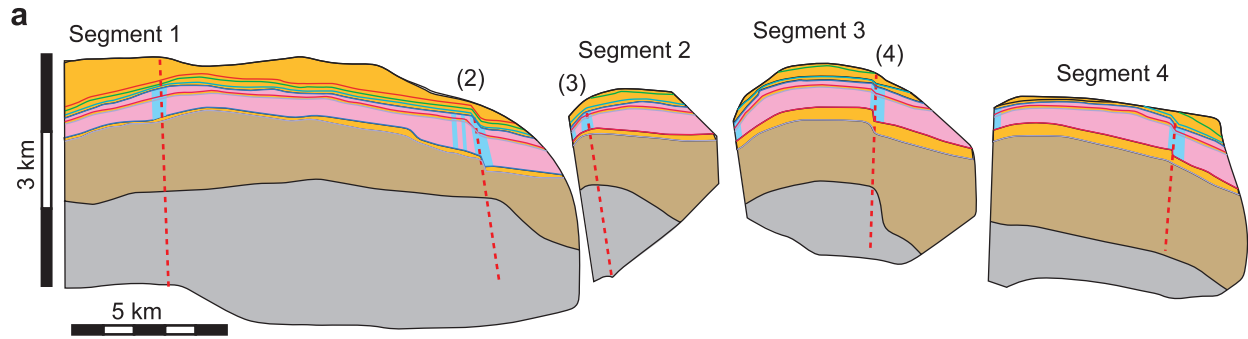
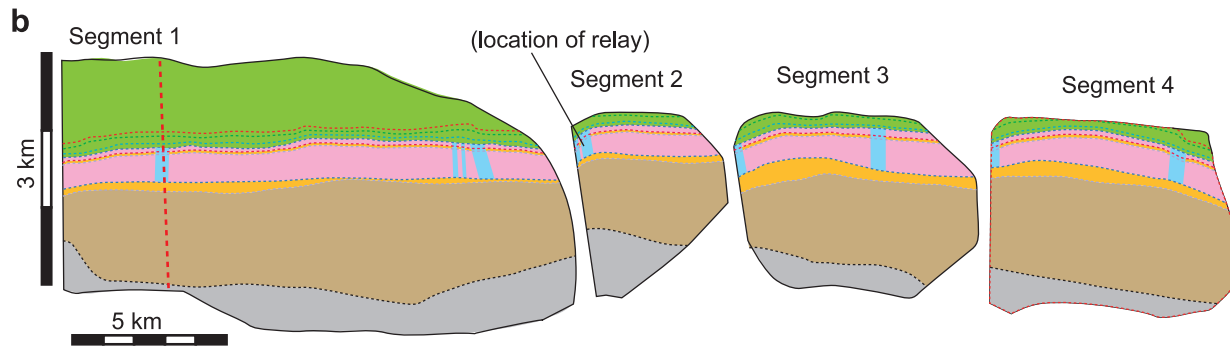


FIGURE 11. Cross sections along the Moab fault showing the dip-parallel distribution of different types of fault zone structures resulting from distinct faulting mechanisms as well as lateral variations in sandstone thickness associated with fault segmentation. Locations of sections (a–d) are indicated in Figure 10. Note that abbreviations of stratigraphic names are defined in Figure 2.

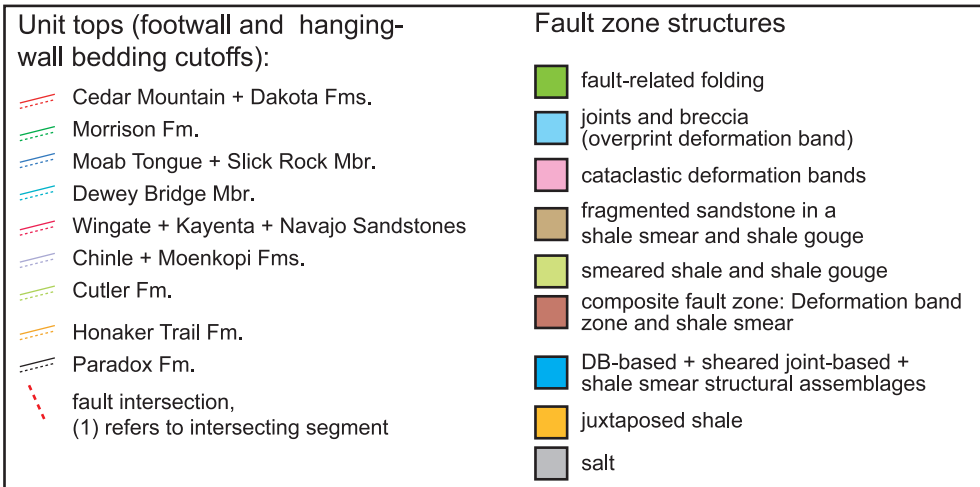
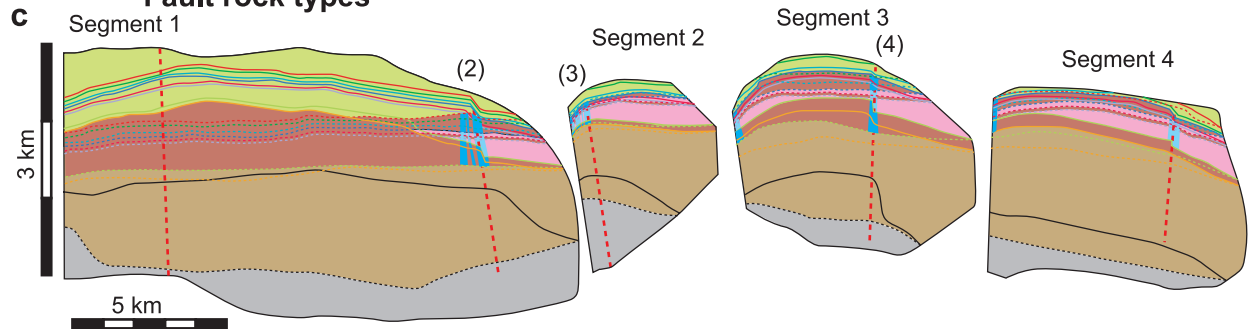
Footwall structures



Hanging-wall structures



Fault rock types



DISCUSSION

Shale Deformation

Shale deformation associated with the Moab fault is dominated by folding and smearing similar to that described by many previous workers (Weber et al., 1978; Lehner and Pilaar, 1997; Aydin and Eyal, 2002; Koledoye et al., 2000). Relatively compliant shale units experience pervasive ductile extension and attenuation, which preserves bedding, as well as rotation of bedding to subparallelism with fault slip surfaces. Concurrently, gouge develops along the contact between the shale smear and fault slip surface. Gouge development suggests frictional wear along the contact of the fault surfaces with smeared shale; this process might contribute to thinning of the smeared shale as offset increases. Shale-related fault rocks are limited to the region between the footwall and hanging-wall sources of shale, which is consistent with the entrainment of shale into the fault core by either ductile attenuation or abrasion. Both processes probably contributed to the thinning of shale in the fault core. The measurements of smear width (Figure 9) and the field examples (e.g., Figures 5–7) indicate that individual shale units eventually attenuate to zero thickness as the distance from the source of shale becomes large at a large throw. Empirically, our estimates for the maximum distance from the source of shale and the throw that shale persists in the fault zone are consistent with the findings of other workers (Lindsay et al., 1993; Gibson, 1994; Aydin and Eyal, 2002). Because shale is primarily derived from shale units in the hanging wall, the gap in the shale smear will most likely first appear closer to the footwall cutoff.

Shale fault rocks persist in the fault core for relatively large distances from the source of shale and demonstrate a consistently low rate of thinning with distance from the source of shale (Figure 9). This might be explained if the fault core continues to incorporate shale from the source units into the smear as throw increases. For example, in Figure 4b, extension of the shale layer is observed well into the hanging wall. Similarly, shale layers in folds illustrated in Figure 7 thin toward the fault slip surface by extension parallel to bedding. This thinning and extension of the source layers adjacent to the fault might indicate that shale is extracted from the source layer into the fault core over a significant distance from the fault surface, providing a long-lasting supply of shale to the smear. Alternatively, broad fold hinges could increase the area that shale is juxtaposed against the fault and thus might contribute

more shale to the fault rock, especially if the wear process is the primary mechanism of fault rock development. Both processes imply that the thickness of the sources of shale should be a significant controlling parameter. However, the measurements in Figure 9 and Table 2 do not clearly support this supposition.

A simpler possibility is that the smeared shale is uniformly thinned and spread out over a proportionately larger area as fault offset increases. This process requires no additional shale as the fault develops but does suggest that the initial input of shale into the fault zone is a primary control on the evolution of smear thickness. As a result, the shale smear would become discontinuous at an offset largely determined by the initial volume of shale in the fault zone. In turn, the initial volume of shale could be controlled by the geometry of the relay that initially forms around the smear (e.g., Figure 5). Thus, some of the variability in the measurement of smear width (Figure 9) could be attributed to the geometry of the fault system during an early stage of development.

In addition to geometric parameters, the competency contrast (Goodwin and Tikoff, 2002) and ductility contrast (Sperrevik et al., 2000; Clausen and Gabrielsen, 2002) between shale and sandstone units have been identified as important factors that determine what units can smear. The ductility of shale units might also impact the length and continuity of the smear from the source of shale. These properties will evolve because of compaction during burial, changes in the water content, and diagenesis of shale units and, thus, might be different at different burial depths or change during the life of the fault. Furthermore, Takahashi (2003) noted that the persistence of low cross-fault permeability in experimentally deformed samples containing a fine-grained layer depended on the effective normal stress. As offset increased, low permeability across the fault and the continuity of the fault seal persisted to greater throw when the effective normal stress was greater. These changes will ultimately determine the processes involved in faulting that can contribute to the sealing of faults.

Implications for Faults and Fluid Flow

The criteria used to estimate the sealing potential of a fault zone largely depend on the objective of the fault zone evaluation. For instance, if seal capacity for hydrocarbon trapping is estimated by the capillary entry pressure (Watts, 1987; Knipe et al., 1998) or failure by hydrofracture, then the simple presence or absence of shale and its petrophysical properties are the limiting

FIGURE 12. Fault plane diagrams depicting the distribution of fault zone components in the (a) footwall, (b) hanging wall, and (c) fault core. Fault planes are projected onto a vertical plane trending 315°. The vertical scale is exaggerated 2.5× the horizontal scale. Fault segments are numbered in the index map of Figures 7, 9, and 11.

factors. Conversely, if fluid flux is the limiting parameter, then the thickness of shale in the fault zone, its permeability, and the time interval are major limiting factors.

At the Moab fault, available outcrop evidence suggests that shale fault rock is continuous without physical gaps or windows. Consequently, sandstone beds internal to thick shale packages are highly unlikely to be directly juxtaposed against other sandstone units across the fault zone. Thus, communication of fluid from footwall sandstone units into sandstone units in the hanging wall would be inhibited by shale. This isolation would prevent charging of sandstone units in the hanging wall with hydrocarbons derived from outside the footwall side.

A similar case for fault sealing can be made for the distribution of deformation bands in the fault zone. Along the Moab fault, we argue that some minimum thickness of deformation bands is likely for a given throw (Davatzes, 2003), although the actual density and width of the zone are highly variable and may be much greater. Thus, the deformation bands present the potential to inhibit fluid flow across the fault and, in some circumstances, can be evaluated as a seal, or at least a baffle, to fluid flux.

In contrast, joint and breccia development near intersections in relays and in folded sandstone units of the Salt Wash Member along the fault system overprint deformation bands, suggesting the potential for increased permeability in these regions. This hypothesis is corroborated by oil staining, intense calcite and ankerite precipitation, and bleaching (Foxford et al., 1996) in the Entrada Formation at these locations, which we interpret to result from enhanced fluid flux. Thus, joint-based structures might have mitigated the impact of deformation bands in sandstone but might not breach shale seals unless the shale is very thin and the stress state is reasonable for hydrofracture. Local stress perturbations caused by slip on the fault segments that promote dilation at these locations are consistent with the distribution of joint-based structures (Davatzes, 2003). We were unable to directly observe evidence in the shale-rich units at these locations for joint-related structures. However, Foxford et al. (1998) does document the presence of veins at some locations within shale.

These effects are localized in the different parts of the fault zone, including the fault core and the damage zones (Figure 12), and thus, these zones may have disparate hydrologic properties. For instance, the fault core might be sealing, whereas the damage zone on either side of the fault may have enhanced permeability because of joint development (Figures 10, 11). Conversely, a permeable fault core may be bounded by shale or dense deformation band zones on one or both sides, resulting in an isolated fluid conduit such as at the relay indicated in Figure 12 and along portions of fault intersections.

Extrapolating Fault Architecture Using Faulting Mechanisms

Similar to most large, long-lived faults cutting a complicated stratigraphic package of sandstone and shale, the Moab fault system displays complex fault architecture with structures derived from many different faulting mechanisms. We have been able to identify specific parameters, including the stratigraphy (distribution and petrophysics of rock types), fault geometry, slip distribution, and deformation conditions, that controlled the involvement of these mechanisms during development of the Moab fault zone. These parameters provide criteria that can be used to predict or extrapolate the fault architecture from limited data sets common in petroleum exploration and production. As a result, we were able to map the distribution of different types of structures onto the fault plane diagram in Figure 12 and extrapolate them from surface observations along fault dip.

We suggest that this approach is an improvement over purely empirical or statistical approaches to predicting or extrapolating fault zone architecture because it can be checked for self-consistency, requires physically plausible structural assemblages, and is capable of predicting abrupt changes in fault characteristics. For instance, Foxford et al. (1998), who assessed the architecture of the Moab fault, tested the relationship between fault offset and the distribution of fault rocks. They found little consistency and, thus, predictability in the fault architecture. In analyzing the data, they did not consider the distance from potential sources of shale or the effects of fault geometry, such as intersections and relays. As a result, their data set makes it difficult to determine why so little correlation exists between parameters like throw and fault zone width or whether there should be. However, their results importantly emphasize that the spatial proximity of two data points does not insure similar properties. Furthermore, this problem will be compounded where data, samples, and observations are limited (e.g., boreholes, seismic, or other remote sensing data). Thus, changes in fault architecture that occur in small regions, such as joint development localized around intersections and some relays, will either be missed by this approach or remain unexplained.

In contrast, the criteria we have outlined have logical relationships to the faulting mechanisms. As a result, the potential for joint-based architecture could be tested using mechanical models (Davatzes, 2003) and borehole stress analyses. Furthermore, these predictions can be evaluated in the context of the deformation history to determine the potential temporal evolution of fault architecture, which is not possible using most statistical methods. For instance, at the Moab fault, joints postdate deformation bands, where both structures occur,

and are associated with localized fluid flux. These circumstances indicate a change in faulting mechanism that produced a corresponding change in the hydraulic properties of the fault. Numerical simulations indicate that this might have occurred during a late stage of fault development, as the faults grow larger and interact, or if faulting continues into a period of exhumation (Davatzes, 2003). Thus, the potential for a faulted reservoir to charge with hydrocarbons could be linked not only to the timing of fault development but also to the evolution of fault properties. Finally, these logical relationships help clarify when uncertainty in controlling parameters might make an analysis of fault architecture difficult.

A variety of sources of error in this analysis must be mentioned because they impact the reliability of using faulting mechanisms to extrapolate fault zone properties. This analysis is sensitive to the geometry of the fault system and the faulted stratigraphy. In our study, the outcrop trace of the fault is very well constrained. However, salt redistribution during sedimentation leads to highly variable formation thickness. As a result, estimates of fault throw, unit juxtaposition across the fault, and the thickness of shale as a source for fault rock each has an associated uncertainty that increases with depth. In addition, folding is common in the shale-dominated units of the hanging wall of the Moab fault (Figure 7). Such folding has a profound impact on the construction of juxtaposition diagrams and the potential distribution of smeared shale. Because folding occurs within only a few hundred meters of the fault, it will be difficult to image in subsurface cases that rely on seismic data sets.

Similarly, downdip fault geometry is not well constrained. As a result, we assumed the simplest geometry while honoring surface data and available wells. Thus, the fault core is idealized as a single plane for the purpose of visualization and because of the resolution of downdip data. This assumption is of particular interest because the process of shale smear (Figure 4c) suggests vertical fault segmentation at a much smaller scale compared to the fault height and offset. Thus, we are aware of vertical segmentation, having observed it in some locations, but recognize that it is difficult to predict in the subsurface without very detailed, reliable stratigraphic data. In addition, the relative thickness of sandstone and shale seems to have affected the folding behavior of the stratigraphic package. Intervals of thicker sandstone and thinner shale are associated with small fold amplitudes and narrow hinges and a narrower fault zone. In some cases (e.g., Figure 7; station J1), sandstone layers abruptly truncate with the result that the fault zone is uncommonly wide in these regions for short distances along dip. Thus, sedimentological variation in the relative thickness of interbedded sand-

stone and shale in units such as the Salt Wash Member could control the local variation of shale smear thickness.

CONCLUSIONS

Three deformation mechanisms contributed to the development of the Moab fault, resulting in structural heterogeneity along the fault zone. Sandstone deformation is accommodated by the formation of deformation bands and related slip surfaces. At intersections and relays and in thin beds of folded sandstone layers, joints and sheared joints overprint deformation bands. In locations faulted past shale-rich stratigraphic horizons, shale smear and gouge, as well as fragmentation of sandstone layers, are prevalent fault zone components. Individual shale units persist as much as eight times their bed thickness along the fault zone, although shale smear thickness is highly variable along strike and dip. The development of these three types of structural assemblages suggests that the temporally and spatially variable architecture of the Moab fault should have behaved as a complex barrier and conduit system with a major impact on subsurface fluid flow. In addition, despite the complexity of the fault system, Figure 12 illustrates that the distribution of structures resulting from all three faulting mechanisms follows a consistent pattern related to the stratigraphy, juxtaposition, throw, and fault geometry. The present architecture of the fault demonstrates that faulting processes provide a self-consistent, physically realistic basis to interpolate the architecture of a fault zone in poorly constrained locations. Furthermore, this approach makes it possible to identify the sources of uncertainty that affect each faulting mechanism and thus assess the reliability of a sealing analysis.

ACKNOWLEDGMENTS

We acknowledge the financial support of the Rock Fracture Project in the Geological and Environmental Science Department at Stanford University. Useful feedback and discussions were provided by Peter Eichhubl. We also thank Bill Dunne, Jonathan Caine, Rasoul Sorkhabi, and Jennifer Wilson for careful reviews of the manuscript, which helped us improve the clarity of the presentation.

REFERENCES CITED

- Allan, U. S., 1989, Model for hydrocarbon migration and entrapment within faulted structures: AAPG Bulletin, v. 73, p. 803–811.

- Anderson, T. L., 1995, *Fracture mechanics: Fundamentals and applications*, 2d ed.: New York, CRC Press, 688 p.
- Antonellini, M., and A. Aydin, 1994, Effect of faulting on fluid flow in porous sandstones; petrophysical properties: *AAPG Bulletin*, v. 78, no. 3, p. 355–377.
- Antonellini, M., and A. Aydin, 1995, Effect of faulting on fluid flow in porous sandstones; geometry and spatial distribution: *AAPG Bulletin*, v. 79, no. 5, p. 642–671.
- Antonellini, M., A. Aydin, and L. Orr, 1999, Outcrop-aided characterization of a faulted hydrocarbon reservoir: Arroyo Grande oil field, California, U.S.A., *in* W. C. Haneberg, P. S. Mozley, J. C. Moore, and L. B. Goodwin, eds., *Faults and subsurface fluid flow in the shallow crust: American Geophysical Union Geophysical Monograph 113*, p. 7–26.
- Aydin, A., 2000, Fractures, faults, and hydrocarbon entrapment, migration and flow: *Marine and Petroleum Geology*, v. 17, p. 797–814.
- Aydin, A., and Y. Eyal, 2002, Anatomy of a normal fault with shale smear: Implications for fault seal: *AAPG Bulletin*, v. 86, no. 8, p. 1367–1381.
- Aydin, A., and A. M. Johnson, 1978, Development of faults as zones of deformation bands and as slip surfaces in sandstone: *Pure and Applied Geophysics*, v. 116, p. 931–942.
- Bredehoeft, J. D., W. Back, and B. B. Hanshaw, 1982, Regional ground-water flow concepts in the United States; historical perspective, *in* T. N. Narasimhan, ed., *Recent trends in hydrogeology: Geological Society of America Special Paper 189*, p. 297–316.
- Brace, W. F., and E. G. Bombolakis, 1963, A note on brittle crack growth in compression: *Journal of Geophysical Research*, v. 68, no. 12, p. 3709–3713.
- Caine, J., J. Evans, and C. Forster, 1996, Fault zone architecture and permeability structure: *Geology*, v. 24, no. 11, p. 1025–1028.
- Caine, S. C., and C. B. Forster, 1999, Fault zone architecture and fluid flow: insights from field data and numerical modeling, *in* W. C. Haneberg, P. S. Mozley, J. C. Moore, and L. B. Goodwin, eds., *Faults and subsurface fluid flow in the shallow crust: American Geophysical Union Geophysical Monograph 113*, p. 101–127.
- Chester, F. M., and J. M. Logan, 1986, Implications for mechanical properties of brittle faults from observations of the Punchbowl fault zone, California: *Pure and Applied Geophysics*, v. 124, p. 77–106.
- Clausen, J. A., and R. H. Gabrielsen, 2002, Parameters that control the development of clay smear at low stress states: An experimental study using ring-shear apparatus: *Journal of Structural Geology*, v. 24, p. 1569–1586.
- Cruikshank, K. M., and A. Aydin, 1994, Role of fracture localization in arch formation, Arches National Park, Utah: *Geological Society of America Bulletin*, v. 106, no. 7, p. 879–891.
- Cruikshank, K. M., G. Zhao, and A. M. Johnson, 1991, Analysis of minor fractures associated with joints and faulted joints: *Journal of Structural Geology*, v. 13, no. 8, p. 865–886.
- Davatzes, N. C., 2003, Fault architecture as a function of deformation mechanism in clastic rocks with an emphasis on sandstone: Ph.D. thesis, Stanford University, California, 172 p.
- Davatzes, N. C., and A. Aydin, 2003, Overprinting faulting mechanisms in high porosity sandstones of SE Utah: *Journal of Structural Geology*, v. 25, no. 11, p. 1795–1813.
- Dholakia, S. K., A. Aydin, D. D. Pollard, and M. D. Zoback, 1998, Fault-controlled hydrocarbon pathways in the Monterey Formation, California: *AAPG Bulletin*, v. 82, no. 8, p. 1551–1574.
- Doelling, H. H., 1982, Stratigraphic investigations of Paradox basin structures as a means of determining the rates and geologic age of salt-induced deformation: A preliminary study: *Utah Geologic and Mineral Survey Open-file Report 29*, 88 p., 9 plates.
- Doelling, H. H., 1985, *Geology of Arches National Park: Utah Geological and Mineral Survey, Map 74*, 2 sheets, scale 1:50,000.
- Doelling, H. H., 1988, *Geology of Salt Valley anticline and Arches National Park, Grand County, Utah*, *in* H. H. Doelling, C. G. Oviatt, and P. W. Huntoon, eds., *Salt deformation in the Paradox region: Utah Geological and Mineral Survey, Salt Lake City, Utah, Bulletin*, v. 122, p. 7–58.
- Doelling, H. H., 2002, *Geologic map of the Moab and eastern part of the San Rafael desert 30/X 60' quadrangles, Grand and Emery Counties, Utah, and Mesa County Colorado: Utah Geological Survey Map 180*, scale 1:100,000, 3 plates.
- Dyer, J. R., 1983, *Jointing in sandstones, Arches National Park, Utah: Ph.D. thesis, Stanford University, Stanford, California 275 p.*
- Eichhubl, P., and J. Boles, 2000, Focused fluid flow along faults in the Monterey Formation, coastal California: *Geological Society of America Bulletin*, v. 112, no. 11, p. 1667–1679.
- Engelder, J. T., 1987, Joints and shear fractures in rock, *in* B. K. Atkinson, ed., *Fracture mechanics of rock: London, Academic Press*, p. 27–69.
- Faulkner, D. R., and E. H. Rutter, 1998, The gas permeability of clay-bearing fault gouge under high pressure at 20°C: *Journal of Geophysical Research*, v. 105, no. 7, p. 16,415–16,426.
- Flodin, E. A., 2003, *Structural evolution, petrophysics, and large-scale permeability of faults in sandstone, Valley of Fire, Nevada: Ph.D. thesis, Stanford University, California, 180 p.*
- Flodin, E. A., A. Aydin, L. J. Durlofsky, and B. Yeten, 2001, Representation of fault zone permeability in reservoir flow models, *in* *Society of Petroleum Engineers Annual Technical Conference and Exhibition, New Orleans, SPE Paper 71671*, 10 p.
- Foxford, K. A., I. R. Garden, S. C. Guscott, S. D. Burley, J. J. M. Lewis, J. J. Walsh, and J. Waterson, 1996, The field geology of the Moab fault, *in* A. C. Huffman, W. R. Lund, and L. H. Goodwin, eds., *Geology and resources of the Paradox basin: Salt Lake City, Utah, Utah Geological Association Guidebook*, v. 25, p. 265–283.
- Foxford, K. A., J. J. Walsh, J. Waterson, I. R. Garden, S. C.

- Guscott, S. D. Burley, Q. J. Fisher, and R. J. Knipe, 1998, Structure and content of the Moab fault zone, Utah, U.S.A., and its implications for fault seal prediction, *in* G. K. Jones, Q. J. Fisher, and R. J. Knipe, eds., *Faulting, fault sealing and fluid flow in hydrocarbon reservoirs: Geological Society (London) Special Publication 147*, p. 87–103.
- Fristad, T., A. Groth, G. Yielding, and B. Freeman, 1997, Quantitative seal prediction: A case study from Oseberg Syd, *in* P. Møller-Pedersen and A. G. Koestler, eds., *Hydrocarbon seals: Importance for exploration and production: Norwegian Petroleum Society Special Publication 7*, p. 107–124.
- Garden, I. R., S. C. Guscott, S. D. Burley, K. A. Foxford, J. J. Walsh, and J. Marshall, 2001, An exhumed palaeo-hydrocarbon migration fairway in the Entrada Sandstone of SE Utah, U.S.A.: *Geofluids*, v. 1, no. 3, p. 195–213.
- Gibson, R. G., 1994, Fault-zone seals in siliciclastic strata of the Columbus basin, offshore Trinidad: *AAPG Bulletin*, v. 78, no. 9, p. 1372–1385.
- Goodwin, L. B., and B. Tikoff, 2002, Competency contrast, kinematics, and the development of foliations and lineations in the crust: *Journal of Structural Geology*, v. 24, p. 427–444.
- Granier, T., 1985, Origin, damping, and pattern of development of faults in granite: *Tectonics*, v. 4, no. 7, p. 721–737.
- Heynekamp, M. R., L. B. Goodwin, P. S. Mozley, and W. C. Haneberg, 1999, Controls on fault-zone architecture in poorly lithified sediments, Rio Grande Rift, New Mexico; implications for fault-zone permeability and fluid flow, *in* W. C. Haneberg, P. S. Mozley, J. C. Moore, and L. B. Goodwin, eds., *Faults and subsurface fluid flow in the shallow crust: American Geophysical Union Geophysical Monograph 113*, p. 27–49.
- Jourde, H., E. Flodin, A. Aydin, L. Durlafsky, and X. Wen, 2002, Computing permeability of fault zones in eolian sandstone from outcrop measurements: *AAPG Bulletin*, v. 86, no. 7, p. 1187–1200.
- Knipe, R. J., 1993, The influence of fault zone processes and diagenesis on fluid flow, *in* A. D. Horbury and A. G. Robinson, eds., *Diagenesis and basin development: AAPG Studies in Geology 36*, p. 135–148.
- Knipe, R. J., 1997, Juxtaposition and seal diagrams to help analyze fault seals in hydrocarbon reservoirs: *AAPG Bulletin*, v. 81, no. 2, p. 187–195.
- Knipe, R. J., G. Jones, and Q. J. Fisher, 1998, Faulting, fault sealing, and fluid flow in hydrocarbon reservoirs; an introduction, *in* G. Jones, Q. J. Fisher, and R. J. Knipe, eds., *Faulting, fault sealing and fluid flow in hydrocarbon reservoirs: Geological Society (London) Special Publication 147*, p. vii–xxi.
- Koledoye, A. B., A. Aydin, and E. May, 2000, Three-dimensional visualization of normal fault segmentation and its implication for fault growth: *Leading Edge*, v. 19, no. 7, p. 692, 696, 698, 700–701.
- Koledoye, B. A., A. Aydin, and E. May, 2003, A new process-based methodology for analysis of shale smear along normal faults in the Niger Delta: *AAPG Bulletin*, v. 87, no. 3, p. 445–463.
- Lehner, F. K., and W. F. Pilaar, 1991, On a mechanism of clay smear emplacement in synsedimentary normal faults: Inferences from field observations near Frechen, Germany, *in* P. Møller-Pedersen and A. G. Koestler, eds., *Hydrocarbon seals: Importance for exploration and production: Norwegian Petroleum Society Special Publication 7*, p. 39–50.
- Lehner, F. K., and W. F. Pilaar, 1997, The emplacement of clay smears in synsedimentary normal faults: Inferences from field observations near Frechen, Germany, *in* P. Møller-Pedersen and A. G. Koestler, eds., *Hydrocarbon seals: Importance for exploration and production: Norwegian Petroleum Society Special Publication 15*, p. 39–50.
- Lindsay, N. G., F. C. Murphy, J. J. Walsh, J. Watterson, and I. D. Bryant, 1993, Outcrop studies of shale smears on fault surfaces, *in* S. S. Flint, ed., *Geological modeling of hydrocarbon reservoirs and outcrop analogues: International Association of Sedimentologists Special Publication 15*, p. 113–123.
- Martel, S. J., 1990, Formation of compound strike-slip fault zones, Mount Abbot Quadrangle, California: *Journal of Structural Geology*, v. 12, no. 7, p. 869–882.
- Matthai, S. K., A. Aydin, D. D. Pollard, S. G. Roberts, Q. J. Fisher, and R. J. Knipe, 1998, Numerical simulation of departures from radial drawdown in a faulted sandstone reservoir with joints and deformation bands, *in* G. Jones, Q. J. Fisher, and R. J. Knipe, eds., *Faulting, fault sealing, and fluid flow in hydrocarbon reservoirs: Geological Society (London) Special Publication 147*, p. 157–191.
- Myers, R. D., 1999, Structure and hydraulic properties of brittle faults in sandstone: Ph.D. thesis, Stanford University, Stanford, California, 176 p.
- Nelson, E. P., A. J. Kullman, M. H. Gardner, and M. Batzle, 1999, Fault-fracture networks and related fluid flow and sealing, Brushy Canyon Formation, west Texas, *in* W. C. Haneberg, P. S. Mozley, J. C. Moore, and L. B. Goodwin, eds., *Faults and subsurface fluid flow in the shallow crust: American Geophysical Union Geophysical Monograph 113*, p. 69–81.
- Nuccio, V. F., and S. M. Condon, 1996, Burial and thermal history of the Paradox basin, Utah and Colorado, and petroleum potential of the middle Pennsylvanian Paradox basin: *U.S. Geologic Survey Bulletin, Report B 2000-O*, p. O1–O41.
- Pevear, D. R., P. J. Vrolijk, and F. J. Longstaffe, 1997, Timing of Moab fault displacement and fluid movement integrated with burial history using radiogenic and stable isotopes: *Geofluids II Extended Abstracts*, p. 42–45.
- Segall, P., and D. D. Pollard, 1980, Mechanics of discontinuous faults: *Journal of Geophysical Research*, v. 85, no. 8, p. 4337–4350.
- Sibson, R. H., 1977, Fault rocks and fault mechanisms: *Journal of the Geological Society (London)*, v. 133, p. 191–231.
- Sibson, R. H., 1990, Conditions for fault-valve behavior, *in* R. J. Knipe and E. H. Rutter, eds., *Deformation mechanisms, rheology and tectonics: Geological Society (London) Special Publication 54*, p. 15–28.

- Sigda, J. M., L. B. Goodwin, P. S. Mozley, and J. L. Wilson, 1999, Permeability alteration in small-displacement faults in poorly lithified sediments: Rio Grande rift, Central New Mexico, *in* W. C. Haneberg, P. S. Mozley, J. C. Moore, and L. B. Goodwin, *Faults and subsurface fluid flow in the shallow crust: American Geophysical Union Geophysical Monograph 113*, p. 51–68.
- Skerlec, G. M., 1999, Evaluating top and fault seal, *in* E. A. Beaumont and N. H. Foster, eds., *Exploring for oil and gas traps: AAPG Treatise of Petroleum Geology, Handbook of Petroleum Geology*, p. 10-4–10-94.
- Sperrevik, S. R. B., R. B. Faereth, and R. H. Gabreilsen, 2000, Experiments on clay smear formation along faults: *Petroleum Geoscience*, v. 6, p. 113–123.
- Takahashi, M., 2003, Permeability change during experimental fault smearing: *Journal of Geophysical Research*, v. 108, no. 5, p. 2235–2250.
- Taylor, W. L., D. D. Pollard, and A. Aydin, 1999, Fluid flow in discrete joint sets; field observations and numerical simulations: *Journal of Geophysical Research*, v. 104, no. 12, p. 28,983–29,006.
- Watts, N. L., 1987, Theoretical aspects of cap-rock and fault seals for single- and two-phase hydrocarbon columns: *Marine and Petroleum Geology*, v. 4, p. 274–307.
- Weber, K. J., G. Mandl, F. Pilaar, F. K. Lehner, and R. G. Precious, 1978, The role of faults in hydrocarbon migration and trapping in Nigerian growth fault structures, *in* American Institute of Mining Metallurgical and Petroleum Engineers and Society of Petroleum Engineers Tenth Annual Offshore Technology Conference Proceedings, v. 4, p. 2643–2653.
- Yielding, G., B. Freeman, and D. T. Needham, 1997, Quantitative fault seal prediction: *AAPG Bulletin*, v. 81, p. 897–917.